



# Deformation behavior of migmatites: insights from microstructural analysis of a garnet–sillimanite–mullite–quartz–feldspar-bearing anatectic migmatite at Rampura–Agucha, Aravalli–Delhi Fold Belt, NW India

Abhishek Prakash<sup>1</sup> · Sandra Piazzolo<sup>2,3</sup> · Lopamudra Saha<sup>1</sup> · Abhijit Bhattacharya<sup>4</sup> · Durgesh Kumar Pal<sup>5</sup> · Saheli Sarkar<sup>1</sup>

Received: 14 April 2017 / Accepted: 23 February 2018 / Published online: 19 March 2018  
© Springer-Verlag GmbH Germany, part of Springer Nature 2018

## Abstract

In the present study we investigate the microstructural development in mullite, quartz and garnet in an anatectic migmatite hosted within a Grenvillian-age shear zone in the Aravalli–Delhi Fold Belt. The migmatite exhibits three main deformation structures and fabrics ( $S_1$ ,  $S_2$ ,  $S_3$ ). Elongated garnet porphyroblasts are aligned parallel to the metatexite  $S_2$  layers and contain crenulation hinges defined by biotite–sillimanite–mullite–quartz (with  $S_1$  axial planar foliation). Microstructural evidence and phase equilibrium relations establish the garnet as a peritectic phase of incongruent melting by breakdown of biotite, sillimanite ± mullite and quartz at peak  $P$ – $T$  of ~8 kbar, 730 °C along a tight-loop, clockwise  $P$ – $T$  path. Monazite dating establishes that the partial melting occurred between ~1000 and 870 Ma. The absence of subgrains and systematic crystal lattice distortions in these garnets despite their elongation suggests growth pseudomorphing pre-existing 3-D networks of  $S_1$  biotite aggregates rather than high-temperature crystal plastic deformation which is noted in the  $S_1$  quartz grains that exhibit strong crystallographic preferred orientation (CPO), undulatory extinction and subgrains. Mode-I fractures in these garnet porphyroblasts induced by high melt pressure during late stage of partial melt crystallization are filled by retrograde biotite–sillimanite. Weak CPO and non-systematic crystal lattice distortions in the coarse quartz grains within the  $S_2$  leucosome domains indicate these crystallized during melt solidification without later crystal plastic deformation overprint. In the later stages of deformation ( $D_3$ ), strain was mostly accommodated in the mullite–biotite–sillimanite-rich restite domains forming  $S_3$  which warps around garnet and leucosome domains; consequently, fine-grained  $S_3$  quartz does not exhibit strong CPOs.

**Keywords** Melt-present deformation · Anatectic migmatites · Crystal preferred orientation · Quartz · Garnet · Rheology

✉ Lopamudra Saha  
saha.lopmudra@gmail.com

<sup>1</sup> Department of Earth Sciences, Indian Institute of Technology Roorkee, Roorkee 247667, India

<sup>2</sup> Department of Earth and Planetary Sciences, GEMOC ARC National Key Centre and ARC Centre of Excellence Core to Crust Fluid Systems (CCFS), Macquarie University, Sydney, NSW 2109, Australia

<sup>3</sup> School of Earth and Environment, University of Leeds, Leeds LS2 9JT, UK

<sup>4</sup> Department of Geology and Geophysics, Indian Institute of Technology Kharagpur, Kharagpur 721302, India

<sup>5</sup> AMETEK Instruments India Pvt. Ltd, Indian Institute of Technology (Indian School of Mines), Dhanbad, Dhanbad 826004, India

## Introduction

Anatectic migmatites record signatures of partial melting events in mid- to deep-crustal levels at the roots of orogenic belts (Ashworth 1985; Brown 2001; Whitney et al. 2004; Beaumont et al. 2006). The restitic parts preserved in many migmatites are archives of the geological history that pre-dates the melting event (Guernina and Sawyer 2003; Sawyer 2008). Both experimental and theoretical works demonstrate that the dynamic viscosity of partially molten rocks is reduced by several orders of magnitude depending on the volume fraction of melt (Arzi 1978; Vigneresse et al. 1996; Berger and Kalt 1999; Takeda and Obata 2003). Therefore, in situations, where the production, segregation and emplacement of melts are synchronous with active

deformation, strain is likely to be complexly partitioned into low-viscosity melt-dominated layers within the deforming matrix of the bulk rock. However, in such experiments strain rates and temperatures are unrealistic thus experimental results may not be directly applied to study deformation patterns in migmatites (Paterson 1987; Rutter and Neumann 1995). Consequently, detailed studies of natural migmatites are crucial.

Deformation microstructures in minerals in anatectic migmatites in melt-dominated and melt-absent domains can be determined from quantitative orientation analysis including internal deformation features (e.g., subgrains) and their CPOs using electron backscatter diffraction (EBSD) studies (Venables and Harland 1973; Prior et al. 1999; Kleinschrodt and Duyster 2002; Ji et al. 2003; Mainprice et al. 2004; Storey and Prior 2005; Hasalová et al. 2008; Menegon et al. 2011; Cavalcante et al. 2013). The results of such EBSD studies may be combined with quantitative phase equilibrium modeling of melting reactions in migmatites to understand how naturally occurring minerals respond to far-field stress before, at and after supra-solidus conditions. In this study, we integrate the results of phase equilibrium modeling of anatectic migmatites using  $P$ – $T$  pseudosection modeling and EBSD studies in a garnet–biotite–mullite migmatite of the Bhilwara Supergroup (Fig. 1a) from a Grenvillian-age, Northern Indian shear zone to demonstrate the complex interplay between deformation strain, mineralogical reactions and crystallization microstructures developed in quartz, mullite and garnet at subsolidus and supra-solidus condition.

## Geological background and field relationships

The chosen field area lies in the Bhilwara Supergroup of Northern India (Fig. 1a). The Bhilwara Supergroup rocks are exposed along the central and eastern parts of Aravalli–Delhi Fold Belt (Raja Rao 1976; Gupta et al. 1980, 1997, Fig. 1b). Two distinct NNE–SSW trending belts constitute the Bhilwara Supergroup: (1) the western Meso- to Neoproterozoic amphibolite facies schist belt that extends from Rajpura–Dariba in the southwest to Pur–Banera in the northeast and the (2) eastern migmatite belt that extends up to the volcano-sedimentary successions of the Hindoli Group and Jahazpur Belt in the east, the granitoids and metasedimentary units of the North Delhi Fold Belt in the north (Fig. 1b; Gupta et al. 1997). The western schist belt consists of an interlayered sequence of garnet–staurolite–kyanite mica schists, calc-silicate gneisses and quartzites (Hazarika et al. 2013; Ojha et al. 2016). The garnet–sillimanite–biotite gneiss from which the sample studied stems forms the dominant lithology of the eastern

anatectic migmatite belt and is associated with porphyritic granitoid plutons (Hazarika et al. 2013). The Archaean (~2.5 Ga) Berach granite (also called Banded Gneissic Complex, BGC-I; Heron 1953) and the ~Palaeoproterozoic greenschist facies metasedimentary units of the Aravalli Supergroup defines the southern margin of Bhilwara Supergroup. Along their western margin, the migmatites of Bhilwara Supergroup share a NNE-trending tectonic contact (marked by ductile shear zones) with the polycyclic Meso- to Neoproterozoic granulites of the Mangalwar Complex and Sandmata Complex (together forming BGC-II, Heron 1953). Raja Rao (1976) and Gupta et al. (1980, 1997) propose the BGC-I to represent the basement for the Bhilwara Supergroup.

Geochronological data from the Bhilwara Supergroup are sparse. A single zircon age of ~1.45 Ga is reported from the mylonitized porphyritic granitoid in Rampura–Agucha (Roy and Jakhar 2002). A Pb–Pb model age of ~1.8 Ga is obtained by Deb and Thorpe (2004) and Deb et al. (1989) for the anatectic metapelites in Rampura–Agucha. Based on U–Th–Pb (total) age determinations, Hazarika et al. (2013) obtained a single age population of ~1.0 Ga in monazites in the pelitic migmatites of the area. However, multiple monazite age populations have been obtained from the garnet–staurolite–kyanite mica schists of the Rajpura–Dariba interpreted to date peak and retrograde metamorphic events (1.87 and 1.62 Ga; Hazarika et al. 2013) and Pur–Banera (1.37 and 1.05 Ga; Ojha et al. 2016).

The field area at Rampura–Agucha lies close to the north-western margin of the migmatite belt (Fig. 1b). It is characterized by an ensemble of calc-silicate gneisses, amphibolites and anatectic garnet–biotite–sillimanite gneisses and mylonitized porphyritic granitoids (Fig. 1c). Three fabric-forming events are recognized in the garnet–biotite–sillimanite migmatites (Fig. 2a). We use a numbering system in accordance with relative age established in the field. The  $S_1$  fabric is noted exclusively as inclusion trails within garnet porphyroblasts (Table 1; Fig. 3a). The first set of mesoscopic fabric ( $S_2$ ) is defined by garnet-bearing leucosomes in a mesocratic matrix dominated by biotite intergrown with sillimanite, and coarse-grained quartz lenticles. The metatextite  $S_2$  layers are co-axially refolded (hook-shaped fold superposition structures are common) by isoclinal  $D_3$  folds and locally developed NNE-trending tight-to-open  $D_4$  folds that plunge towards NNE (Fig. 2a). The axial planar fabric ( $S_3$ ) is mutually indistinguishable from  $S_2$ , except at  $D_3$  fold hinges (Fig. 2b, c). In contrast,  $D_4$  folding does not result in a recognizable fabric.

We selected a representative sample of the neosome part of the metatextite migmatite from a limb of a  $D_3$  fold, with typical garnet-bearing leucosome and restitic fine-grained layers warping around the leucosome layers (Fig. 2b, c). No  $D_4$  deformation features are seen at the sample location.

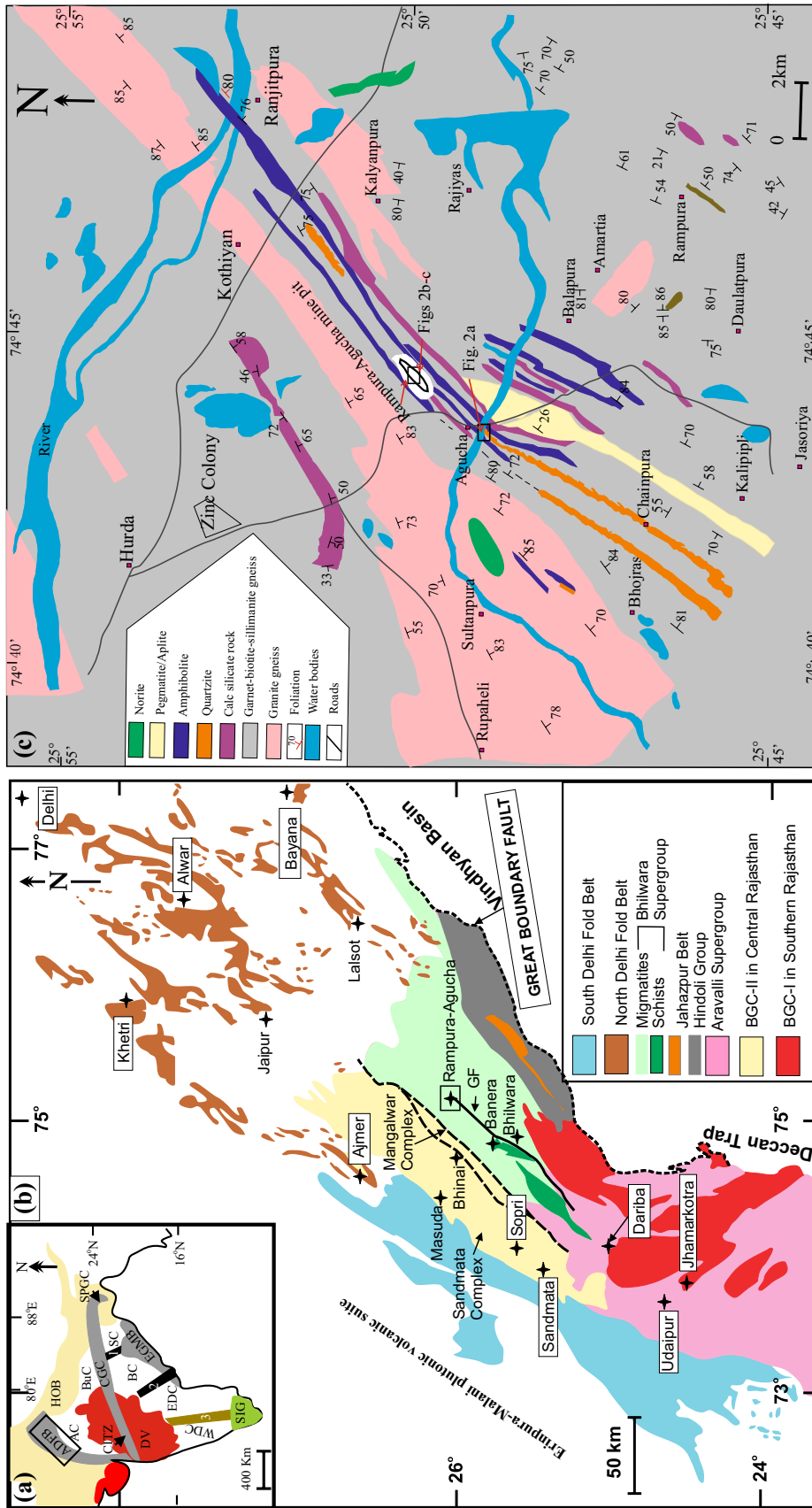


**Fig. 1** a Generalized tectonic map of India showing the Archean cratons and Proterozoic mobile belts. *ADFB* Aravalli Delhi Fold Belt, *AC* Aravalli Craton, *BC* Bundelkhand Craton, *SC* Singhbhum Craton, *BC* Bastar Craton, *EDC* Eastern Dharwar Craton, *WDC* Western Dharwar Craton, *CITZ* Central Indian Tectonic Zone, *CGC* Chotanagpur Gneissic Complex, *SPGC* Shillong Plateau Gneissic Complex, *EGMB* Eastern Ghats Mobile Belt, *SIG* South Indian Granulite terrain, *HOB* Himalayan Orogenic Belt, *DV* Deccan Volcanics; 1 Mahanadi Rift, 2 Godavari Rift, 3 Closepet Granite. Gray regions show the Grenvillian orogenic belt. The study area (*ADFB*) is shown in the box. **b** Map showing different lithological and tectonic components of Aravalli Craton and Aravalli Delhi Fold Belt (modified after Heron 1953; Roy and Jakhar 2002). *GF*: Grenvillian Fold Belt (modified after Roy 2000). Boxes show locations from which detailed structural analyses have been conducted and location (Rampura–Agucha mine pit) from which sample RAM-1 has been collected



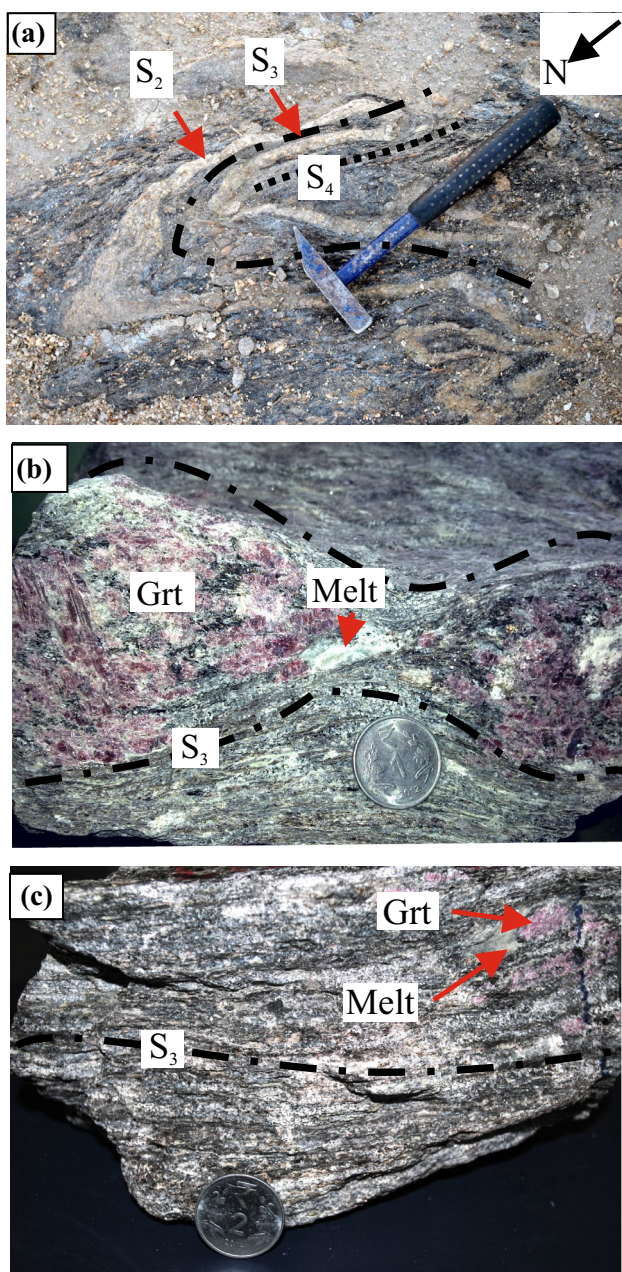


**Fig. 2** **a** Field photograph of anatectic garnet–biotite–sillimanite gneiss showing different stages of deformation (for detailed description see text). **b, c** Photographs showing the neosome parts of anatectic garnet–biotite–sillimanite-bearing migmatite (RAM-1). Mineral abbreviations in the figures and tables are after Kretz (1983). See text for description of structural elements in the rock

## Analytical methods

### Mineral chemistry and bulk chemistry

Mineral–chemical analyses of an anatectic garnet–biotite–sillimanite gneiss (RAM-1; Fig. 2b, c) were carried out with a CAMECA SX (EPMA) at Indian School of Mines,

Dhanbad. Operating conditions for feldspar analyses were acceleration voltage 15 kV with 15 nA beam current, and 15 kV, 20 nA were used for biotite, garnet, sillimanite and ilmenite. In-built ZAF corrections were applied.

For pseudosection modeling, the bulk composition of the sample RAM-1 was determined by X-ray fluorescence at the National Geophysical Research Institute, Hyderabad. The analysis was done using a Phillips MagiX PRO Model 2440 XRF spectrometer.

### Quantitative microstructural analysis and representation

Electron back-scatter diffraction (EBSD) analyses were done at Macquarie University on thin sections (sample RAM-1) cut perpendicular to  $S_2$  foliation ( $Y$ – $X$  plane) and parallel to the fold axis lineation of  $F_3$  ( $X$  direction). Thin sections were carbon coated (~3 nm thick) following mechano-chemical polishing using colloidal silica. Full crystallographic orientation data were collected using automatically indexed EBSD patterns, acquired with an HKL Nordlys Nano high-sensitivity EBSD detector and indexed using the Aztec analysis software (Oxford Instruments). The SEM was run at a high vacuum, with an accelerating voltage of 20 kV, beam current of 8.2 nA, and with an aperture of 70  $\mu\text{m}$  at a working distance of 9.5–10.5 mm. Data were collected on rectangular grids with step size of 5–25  $\mu\text{m}$  (depending on the required spatial resolution of the crystallographic information) using a beam scan. Noise reduction on the raw data was performed following the procedure tested by Piazzolo et al. (2006), Bestmann and Prior (2003) and Prior et al. (2002). In pole figures, data are represented as one point per grain, where a grain is defined as an area completely surrounded by high-angle ( $> 10^\circ$ ) boundaries. Grains which have a mean internal misorientation  $< 1^\circ$  are considered to be strain free (Piazzolo et al. 2006).

### Monazite analyses

Th–U–Pb (total) age determinations in monazites were computed from analytical data obtained using the Cameca SX electron microprobe analyzer at the Indian School of Mines, Dhanbad following the “age calibration” (Petrík and Konecny 2009). These age data are then corrected against an age standard dated by SIMS method (Tomascek et al. 1998). Analytical settings were set as follows: counting times for Pb 150 s, Th 45 s, U 75 s, Y 45 s, and for all other elements 25–35 s; sample current 100–130 nA; beam diameter ~3  $\mu\text{m}$ . Standards used were the following: P—Apatite, Ca—Wollastonite, La—La Glass, Ce—Ce Glass, Eu—Eu Glass, Si—Albite, Y—YAG, Al—Kyanite, Pb—Crocoite, Th—Thorium Glass, U—Uranium Glass, Pr—Pr Glass, Nd—Nd Glass, Sm—Sm Glass, Gd—Gd Glass, Dy—Dy



**Table 1** Characteristics of microstructures and mineral assemblages

Microstructure type (S=foliation, L—lineation, F—fold, D—deformation)	Mineral assemblage	Main features	Metamorphic reactions leading to assemblage and $P$ – $T$ conditions	Inferred deformation mechanism(s)	Additional comments
$D_1$	Mul <sub>1</sub> , Sil <sub>1</sub> , Qtz <sub>1</sub> , Bt <sub>1</sub>	Mul <sub>1</sub> grains forming two limbs of the crenulations included in garnet porphyroblast show contrasting orientations (Figs. 3a, 6a, b) Rootless fold hinge (Figs. 3a, 7a) Qtz <sub>1</sub> shows strong CPO (Fig. 7b, c)	~650–700 °C	Strong CPO indicates activity of prism $\langle c \rangle$ slip with solid-state dislocation creep	High strain persisted before partial melting and formation of gneissic band $S_2$
$D_2$ ; $S_2$	Grt, Qtz <sub>2</sub> , Kfs <sub>2</sub> , Pl <sub>2</sub> , Bt <sub>2</sub> , Mul <sub>2</sub>	Qtz <sub>2</sub> and Kfs <sub>2</sub> present in the pressure shadows of garnet and within the interfolial domains of $S_2$ . Inclusions of rounded Qtz <sub>1</sub> grain in Kfs <sub>2</sub> , bulbous and lobate Qtz <sub>2</sub> grains intergrown with garnet Mode I fractures filled with Bt <sub>4</sub> , Mul <sub>4</sub> are observed in garnet porphyroblasts. (Fig. 3a, d) Absence of subgrain boundaries in garnet. (Fig. 8 a, c) Qtz <sub>2</sub> grains show weak CPOs (Fig. 7 d–g)	Bt <sub>1</sub> + Sil <sub>1</sub> + Qtz <sub>1</sub> + Pl <sub>1</sub> + H <sub>2</sub> O → garnet + melt (crystallized to form Qtz <sub>2</sub> , Kfs <sub>2</sub> ) ~ 725 °C and ~ 8 kbar	Weak CPOs of Qtz <sub>2</sub> resulted due to crystallization from the melt No crystal plastic deformation is noted in garnet Mode I fractures in garnet interpreted to be formed due to high fluid pressure and differential pure shear stresses	Elongated nature of garnet grains is not due to crystal plastic deformation but rather garnet porphyroblasts have replaced pre-existing foliation of Bt <sub>1</sub> , Sil <sub>1</sub> , Mul <sub>1</sub> and Qtz <sub>1</sub> . Weak CPOs of Qtz <sub>2</sub> and fractures in Grt indicate melt-present deformation
$S_3$	Bt <sub>3</sub> , Sil <sub>3</sub> , Mul <sub>3</sub> , Qtz <sub>2</sub> , Qtz <sub>3</sub>	Foliation (Qtz <sub>3</sub> , Bt <sub>3</sub> , Mul <sub>3</sub> ) warps around garnet porphyroblast and leucosome domains. Fig. 3a Fine-grained Qtz <sub>3</sub> interleaved with Bt <sub>3</sub> , Mul <sub>3</sub> show weak CPO (Fig. 7h, i) Mul <sub>3</sub> shows strong CPO (Fig. 6c, d)	≥ 500 °C	Strong CPO of Mul <sub>3</sub> and weak CPO of Qtz <sub>3</sub> (fine-grained) indicate solid-state deformation in former restitic areas	High-strain that prevailed post-anatexis was accommodated by the fine-grained polygonal (prograde) Qtz <sub>3</sub> by diffusion creep

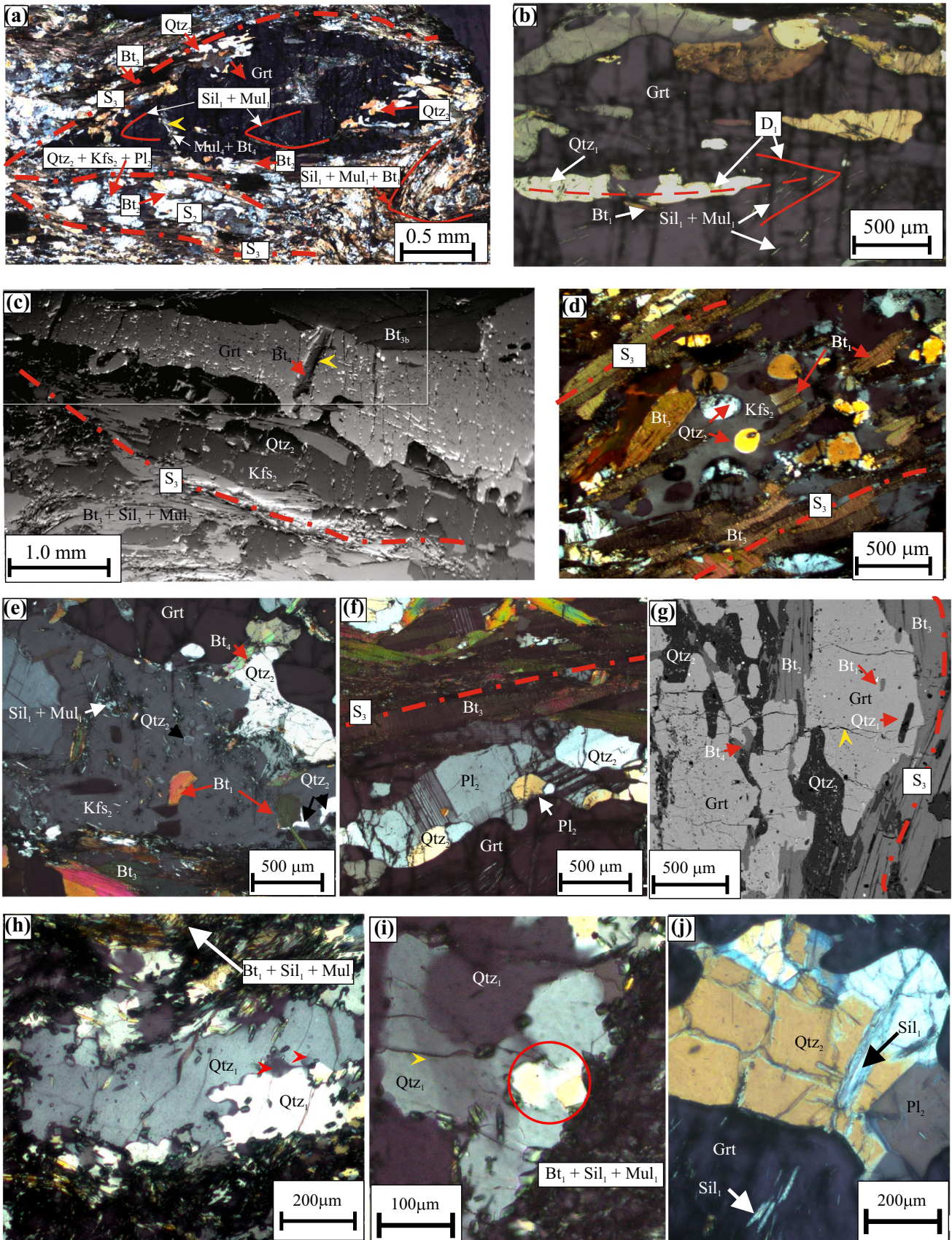




**Fig. 3** Optical microphotographs (**a, b, d–f, h–k**), SEM image (**c**) and BSE image (**g**) displaying textures from RAM-1. **a** Photograph showing  $D_1$  crenulation hinges (defined by sillimanite and mullite) within garnet and pervasive  $S_3$  (defined by biotite, sillimanite, mullite), warping around garnet porphyroblast. Quartz–feldspar-bearing melt layers ( $S_2$ ) occur within the interfolial domains of  $S_3$ . Relict rootless  $D_1$  crenulation hinges occur in the interfolial domains of  $S_3$ ; yellow arrowheads point to fracture filled with biotite and sillimanite/mullite. **b** Garnet porphyroblast preserving  $D_1$  crenulation hinges and quartz inclusion trails axial planar to the crenulation. **c** An elongated garnet porphyroblast in contact with  $S_3$ . **d** A coarse potash feldspar grain (at contact of  $S_3$  biotites), containing rounded quartz inclusions and biotite inclusions. **e** Quartzo-feldspathic layer at contact of garnet porphyroblast showing melt-related microstructures like randomly oriented sillimanite and mullite and biotite grains in coarse potash feldspar, globular inclusions of quartz in potash feldspar and thin melt film (now represented by plagioclase) in between potash feldspar grains. **f** Thin films of plagioclase along the margins of coarser plagioclase indicate sites of melt crystallization. **g** Intergrowth of garnet with globular quartz grains indicates crystallization in presence of melt. **h, i** Coarse quartz grains in the  $D_1$  crenulation hinges are strained, show undulose extinction (yellow arrow) and presence of subgrains (red arrows). **j** Presence of euhedral plagioclase grain at the contact of coarse quartz grains crystallized from melt trapped melt in  $D_2$  garnet. Note presence of relict sillimanite

Glass, Lu—Lu Glass. All errors are given as  $2\sigma$ . Deconvolution histograms were calculated using Isoplot 4.15 (Ludwig 2001).

## Results

### General microstructure phase relationships and mineral chemistry

$S_2$  foliation is defined by alternate melanocratic bands consisting of garnet porphyroblasts, biotite ( $Bt_2$ ), quartz ( $Qtz_2$ ) and leucocratic bands consisting of quartz ( $Qtz_2$ ), plagioclase ( $Pl_2$ ), and potash feldspar ( $Kfs_2$ ; Fig. 3a). Mineralogically similar leucocratic domains are also recognized in the pressure shadows of the garnet porphyroblasts (Table 1; Fig. 3a). Garnet porphyroblasts in the melanocratic bands of the penetrative  $S_2$  metatexite layers are often elongated with aspect ratios of 1.75–3.1 (Figs. 3c, 4). Often bulbous and lobate coarse, strain-free quartz ( $Qtz_2$ ) grains are intergrown with garnets. Fractures within garnet porphyroblasts are oriented perpendicular to porphyroblast elongation (Table 1; Fig. 3c). These fractures in garnet are filled with biotite (Fig. 3c) or biotite–mullite–sillimanite (Fig. 3a). In garnet porphyroblasts  $D_1$  crenulation hinges are mainly defined by mullite ( $Mul_1$ ) and sillimanite ( $Sil_1$ ) (Figs. 3a, b, 4). Inclusion trails of quartz ( $Qtz_1$ ) ribbons and resititic biotite ( $Bt_1$ ) grains are axial planar to these crenulations.  $Qtz_1$  from the relict  $D_1$  hinges in the matrix exhibit undulose extinction and distinct subgrains (Fig. 3h, i). Rootless crenulation hinges (defined by  $Bt_1 + Sil_1 + Mul_1$ ) that

formed during  $D_1$  with orientation similar to those within garnet porphyroblasts also occur in the interfolial domains of  $S_3$  (Fig. 3a). Coarse potash feldspar ( $Kfs_2$ ) grains in the leucocratic layers of  $S_2$  contain sillimanite ( $Sil_1$ ), biotite ( $Bt_1$ ) and quartz ( $Qtz_1$ ) grains (Table 1; Fig. 3d, e). Quartz ( $Qtz_1$ ) inclusions in these potash feldspar ( $Kfs_2$ ) grains are often rounded and form rims around biotite ( $Bt_1$ ) inclusions (Fig. 3e). In leucocratic domains, plagioclase ( $Pl_2$ ) with low dihedral angles occurs at the margins of coarse potash feldspar grains (Fig. 3f). The pervasive foliation in the sample is  $S_3$  which is axial planar to the  $D_3$  folds and transposes  $S_2$ .  $S_3$  is defined by the shape-preferred aggregates of biotite ( $Bt_3$ ), sillimanite ( $Sil_3$ ) and mullite ( $Mul_3$ ) that warp around garnet porphyroblasts in the melanocratic bands of  $S_2$  (Figs. 3a, b, 4; Table 1). In these  $S_3$  domains, quartz is fine grained. The interfolial domains of  $S_3$  consist of the quartz–feldspar-dominated  $S_2$  leucosomes (Figs. 3a, 4), with modally subordinate biotite,  $Bt_2$  (Fig. 3a). To distinguish between the  $Bt + Sil + Mul$  assemblages in the  $S_3$  foliation from those seen in garnet fractures, we label the latter as  $Bt_4 + Sil_4 + Mul_4$  (Fig. 3a, c, g).

$X_{Mg}$  in the cores of garnet porphyroblasts are tightly constrained between 0.19 and 0.20 (Table 2). In contrast, the corresponding values at the rims of the garnet grains (~0.15–0.17) against  $S_3$  biotite ( $Bt_3$ ) and biotites in the fractures are variable, but against quartz grains, the values are identical. Biotite inclusions in garnet ( $Bt_1$ ) and matrix biotite ( $Bt_2$ ) in the  $S_2$  foliation show near-identical  $X_{Mg}$  (0.54 for one  $Bt_1$  analyses and 0.55–0.56 for  $Bt_2$ ) and  $TiO_2$  contents (2.11 pfu for  $Bt_1$  and 1.74–1.99 pfu for  $Bt_2$ ; Table 2).  $X_{Mg}$  and  $TiO_2$  values of coarse biotite grains ( $Bt_3$ ) from the  $S_3$  foliation range from 0.55 to 0.58 and 1.21–2.13 pfu, respectively. The  $X_{Mg}$  values of  $Bt_3$  are similar to that of the  $Bt_1$  and  $Bt_2$ , although their  $TiO_2$  contents show significant variations. Biotites filling the fractures in garnets ( $Bt_4$ ) are richer in Mg than  $Bt_1$ ,  $Bt_2$  and  $Bt_3$ .  $TiO_2$  content of biotites in garnet fractures ( $Bt_4$ ) is in the range 0.1–0.89 pfu (Table 2).

### Mineral paragenetic relationships: their interpretation in terms of succession of geological events

The succession of mineral assemblages that is stable with quartz and plagioclase is shown schematically in Fig. 4. The warping of  $Bt_3 + Sil_3 + Mul_3$  aggregates around garnet porphyroblasts and  $S_3$  continuity indicates pre- $D_3$  garnet (Fig. 3a) growth and fracturing. Coarse K-feldspar ( $Kfs_2$ ) grains in the leucosomes rimming the garnet porphyroblasts, and those occurring in  $S_3$  interfolial domains, host biotite ( $Bt_1$ ), sillimanite ( $Sil_1$ ), and quartz ( $Qtz_1$ ) inclusions, indicating K-feldspar and garnet crystallized from melt (Fig. 3d, e).  $Bt_2$  at the contacts of garnets with globular quartz ( $Qtz_2$ ) grains and with the leucocratic layers of  $S_2$  is also observed



**Fig. 4** Schematic sketch showing deformation microstructures, i.e., **a** D<sub>1</sub> deformation; **b** D<sub>2</sub> deformation; **c** D<sub>3</sub> deformation

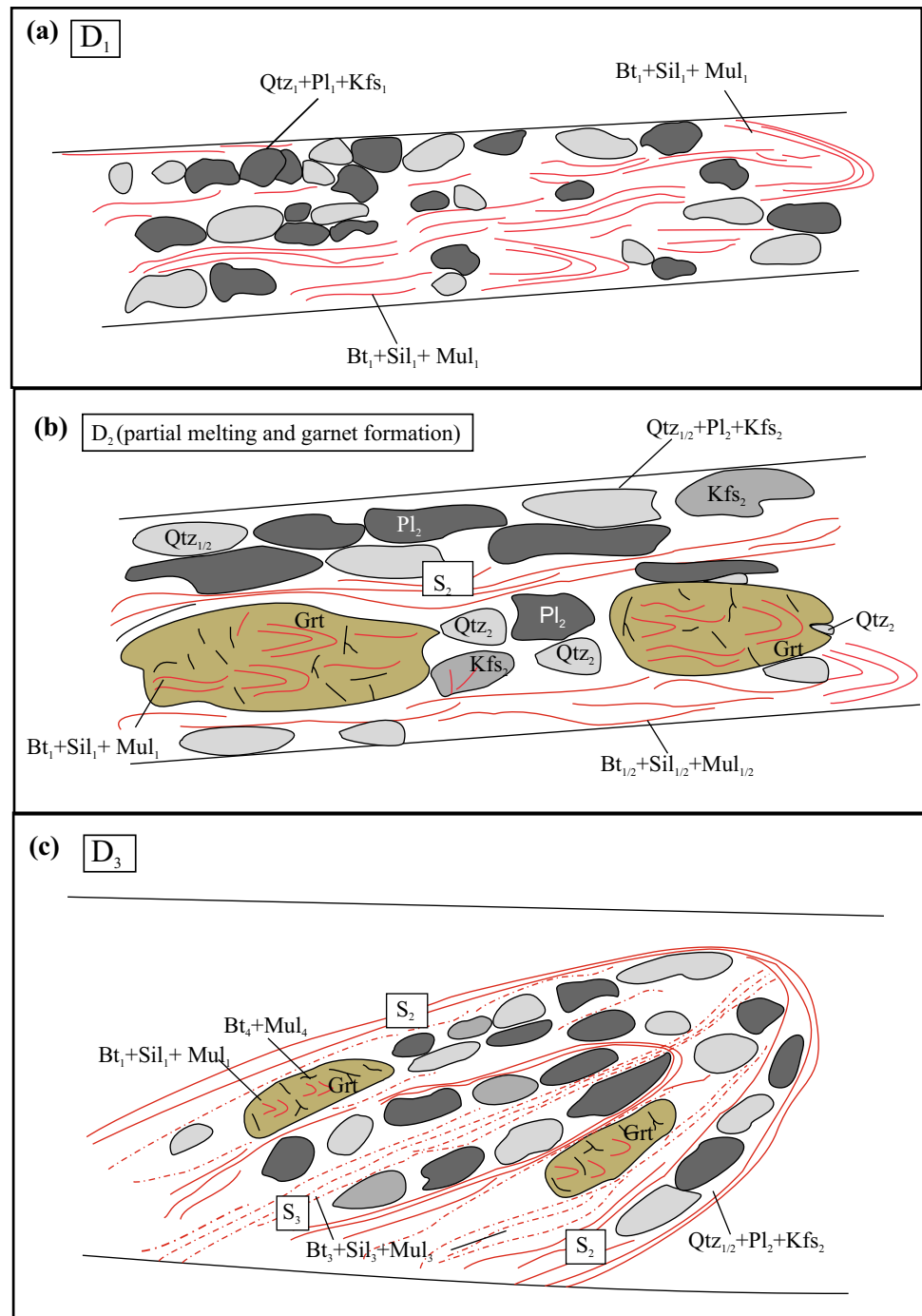


(Fig. 3a, g). The occurrence of garnet within leucocratic domains indicates garnet formation was syn-D<sub>2</sub>. Relict sillimanite (Sil<sub>1</sub>)–mullite (Mul<sub>1</sub>)–biotite (Bt<sub>1</sub>)-bearing crenulation hinges within garnet porphyroblasts, and in the S<sub>3</sub> interfolial domains indicate that these are D<sub>1</sub> deformation features overgrown by D<sub>2</sub> garnet porphyroblasts. The presence of thin films of plagioclase (Pl<sub>2</sub>) around coarse K-feldspar (Kfs<sub>2</sub>) and plagioclase (Pl<sub>1/2</sub>) in the leucosome and the

coarse quartz (Qtz<sub>2</sub>) grains intergrown with garnet corroborate anatexis synchronous with D<sub>2</sub> (Fig. 3e, f). Coarse quartz (Qtz<sub>2</sub>) and plagioclase (Pl<sub>2</sub>) within garnet grains in Fig. 3j are interpreted to have crystallized from trapped melt.

Bt<sub>4</sub> + Sil<sub>4</sub> + Mul<sub>4</sub> assemblages present in garnet fractures or Bt<sub>4</sub> at the contact with garnet margins and at the contacts of garnet and Qtz<sub>2</sub> are interpreted to represent the retrograde assemblage generated by back-reactions of melt in

**Table 2** Representative mineral chemical analyses (EPMA) from RAM-1

Grain 1			Grain 2					Grain 3			
Min	Grt	Grt	Grt	Grt	Grt	Grt	Grt	Grt	Grt	Grt	Grt
	C	R <sup>^</sup> Bt <sub>3</sub>	R <sup>^</sup> Qtz <sub>2</sub>	C	R <sup>^</sup> Bt <sub>4</sub>	C	C	R <sup>^</sup> Qtz <sub>2</sub>	C	C	C
SiO <sub>2</sub>	38.17	37.87	38.2	38.15	37.68	38.19	38.32	38.12	38.31	38.2	38.2
TiO <sub>2</sub>	0.02	0.03	0.11	0	0.02	0	0.01	0	0.03	0	0.05
Al <sub>2</sub> O <sub>3</sub>	20.98	21.12	20.97	20.7	20.5	21.06	20.9	20.93	20.92	21.16	20.82
Cr <sub>2</sub> O <sub>3</sub>	0	0.01	0	0.02	0.04	0.03	0.01	0	0	0	0.01
Fe <sub>2</sub> O <sub>3</sub>	0	0	0	0	0.45	0	0	1.26	0.45	0.92	0.6
FeO	34.95	35.71	34.17	33.89	36.15	34.69	34.6	33.54	34.4	34.09	34.82
MnO	0.51	0.5	0.38	0.38	0.45	0.51	0.46	0.33	0.36	0.41	0.46
MgO	4.48	4.03	4.81	4.77	3.66	4.71	4.53	5.35	5.09	5.14	4.8
CaO	1.37	1.39	1.41	1.4	1.4	1.36	1.34	1.41	1.43	1.39	1.47
Na <sub>2</sub> O	0.05	0.02	0.03	0.06	0.02	0.06	0.02	0.06	0.03	0.05	0
K <sub>2</sub> O	0	0	0	0.01	0.02	0	0	0.03	0.01	0	0
Total	100.53	100.68	100.08	99.38	100.38	100.61	100.19	101.03	101.02	101.36	101.23
Oxygen	12	12	12	12	12	12	12	12	12	12	12
Si	3.027	3.011	3.031	3.047	3.019	3.022	3.042	2.998	3.017	2.998	3.011
Ti	0.001	0.002	0.007	0	0.001	0	0.001	0	0.002	0	0.003
Al	1.961	1.979	1.961	1.949	1.936	1.965	1.956	1.941	1.942	1.958	1.935
Cr	0	0.001	0	0.001	0.003	0.002	0.001	0	0	0	0.001
Fe <sup>3+</sup>	0	0	0	0	0.027	0	0	0.075	0.026	0.055	0.036
Fe <sup>2+</sup>	2.318	2.374	2.267	2.263	2.422	2.296	2.297	2.206	2.265	2.237	2.296
Mn	0.034	0.034	0.026	0.026	0.031	0.034	0.031	0.022	0.024	0.027	0.031
Mg	0.529	0.477	0.569	0.568	0.437	0.555	0.536	0.627	0.597	0.601	0.564
Ca	0.116	0.118	0.12	0.12	0.12	0.115	0.114	0.119	0.121	0.117	0.124
Na	0.008	0.003	0.005	0.009	0.003	0.009	0.003	0.009	0.005	0.008	0
K	0	0	0	0.001	0.002	0	0	0.003	0.001	0	0
Sum	7.995	7.999	7.984	7.984	8	7.999	7.981	8	8	8	8
X <sub>Alm</sub>	0.77	0.79	0.76	0.76	0.80	0.77	0.77	0.74	0.75	0.75	0.76
X <sub>Prp</sub>	0.18	0.16	0.19	0.19	0.15	0.19	0.18	0.21	0.20	0.20	0.19
X <sub>Grs</sub>	0.04	0.04	0.04	0.04	0.04	0.04	0.04	0.04	0.04	0.04	0.04
X <sub>Sps</sub>	0.01	0.01	0.01	0.01	0.01	0.01	0.01	0.01	0.01	0.01	0.01
X <sub>Mg</sub>	0.19	0.17	0.20	0.20	0.15	0.19	0.19	0.22	0.21	0.21	0.20
Grain 3				Grain 4							
Min	Grt	Grt	Grt	Grt	Grt	Grt	Grt	Grt	Grt	Bt <sub>1</sub>	Bt <sub>2</sub>
	R <sup>^</sup> Qtz <sub>2</sub>	R <sup>^</sup> Qtz <sub>2</sub>	C	R <sup>^</sup> Qtz <sub>2</sub>	R <sup>^</sup> Bt <sub>2</sub>	C	C	C	C	I <sup>^</sup> Grt	M(C)
SiO <sub>2</sub>	38.12	38.18	38.17	38.2	37.47	37.69	37.99	37.44	37.68	35.85	35.98
TiO <sub>2</sub>	0	0	0	0	0	0	0	0.02	0	2.11	1.91
Al <sub>2</sub> O <sub>3</sub>	20.43	20.79	20.48	21.06	20.86	20.7	21	20.83	20.74	17.67	17.77
Cr <sub>2</sub> O <sub>3</sub>	0.01	0.04	0.05	0.03	0.06	0.08	0.08	0.1	0	0.01	0.06
Fe <sub>2</sub> O <sub>3</sub>	0.67	0.45	1.22	0.3	0.16	0	0.06	0.73	1.19	0	0
FeO	35.5	36.06	35.46	35.7	32.6	32.67	32.87	32.3	32.06	16.87	17.2
MnO	0.44	0.47	0.47	0.36	0.37	0.31	0.37	0.32	0.42	0.08	0
MgO	4.41	4.29	4.49	4.43	5.57	5.62	5.77	5.78	5.83	11.28	11.7
CaO	1.34	1.15	1.29	1.34	1.39	1.49	1.48	1.45	1.52	0.02	0.03
Na <sub>2</sub> O	0	0	0.01	0	0.02	0	0	0	0.05	0.09	0.18
K <sub>2</sub> O	0.02	0	0	0	0.01	0.02	0	0	0	9.58	9.38
Total	100.94	101.42	101.64	101.42	98.51	98.58	99.62	98.97	99.49	93.56	94.21
Oxygen	12	12	12	12	12	12	12	12	12	11	11

**Table 2** (continued)

Grain 3					Grain 4							Bt <sub>1</sub>	Bt <sub>2</sub>
Min	Grt	Grt	Grt	Grt	Grt	Grt	Grt	Grt	Grt	Grt	Bt <sub>1</sub>	Bt <sub>2</sub>	
	R <sup>^</sup> Qtz <sub>2</sub>	R <sup>^</sup> Qtz <sub>2</sub>	C	R <sup>^</sup> Qtz <sub>2</sub>	R <sup>^</sup> Bt <sub>2</sub>	C	C	C	C	C	I <sup>^</sup> Grt	M(C)	
Si	3.025	3.017	3.011	3.012	3.008	3.022	3.014	2.992	2.996	2.996	2.751	2.742	
Ti	0	0	0	0	0	0	0	0.001	0	0	0.122	0.109	
Al	1.911	1.937	1.904	1.957	1.974	1.957	1.964	1.963	1.944	1.599	1.597		
Cr	0.001	0.002	0.003	0.002	0.004	0.005	0.005	0.006	0	0.001	0.004		
Fe <sup>3+</sup>	0.04	0.027	0.072	0.018	0.009	0	0.003	0.044	0.071	0	0		
Fe <sup>2+</sup>	2.356	2.383	2.339	2.354	2.189	2.191	2.181	2.159	2.132	1.083	1.096		
Mn	0.03	0.031	0.031	0.024	0.025	0.021	0.025	0.022	0.028	0.005	0		
Mg	0.522	0.505	0.528	0.52	0.666	0.672	0.682	0.688	0.691	1.29	1.329		
Ca	0.114	0.097	0.109	0.113	0.12	0.128	0.126	0.124	0.13	0.002	0.002		
Na	0	0	0.002	0	0.003	0	0	0	0.008	0.013	0.027		
K	0.002	0	0	0	0.001	0.002	0	0	0	0.938	0.912		
Sum	8	8	8	8	8	7.998	8	7.999	8	7.804	7.818		
X <sub>Alm</sub>	0.78	0.79	0.78	0.78	0.73	0.73	0.72	0.72	0.72				
X <sub>Prp</sub>	0.17	0.17	0.18	0.17	0.22	0.22	0.23	0.23	0.23				
X <sub>Grs</sub>	0.04	0.03	0.04	0.04	0.04	0.04	0.04	0.04	0.04				
X <sub>Sps</sub>	0.01	0.01	0.01	0.01	0.01	0.01	0.01	0.01	0.01				
X <sub>Mg</sub>	0.18	0.17	0.18	0.18	0.23	0.23	0.24	0.24	0.24	0.54	0.55		
Min	Bt <sub>2</sub>	Bt <sub>2</sub>	Bt <sub>2</sub>	Bt <sub>3</sub>	Bt <sub>3</sub>	Bt <sub>3</sub>	Bt <sub>3</sub>	Bt <sub>3</sub>	Bt <sub>3</sub>	Bt <sub>3</sub>	Bt <sub>3</sub>	Bt <sub>3</sub>	
	M(C)	M(C)	M(C)	M(C)	M(C)	M(C)	M(C)	M(C)	M(C)	M <sup>^</sup> Grt Rim	M <sup>^</sup> Grt Rim	M <sup>^</sup> Grt Rim	
SiO <sub>2</sub>	35.64	35.68	35.57	36.7	36.3	34.72	35.81	36.53	36.37	36.74	36.36	36.32	
TiO <sub>2</sub>	1.87	1.99	1.74	1.88	1.21	1.24	1.18	1.94	2.13	2.21	2	2.13	
Al <sub>2</sub> O <sub>3</sub>	17.93	17.71	17.18	17.55	18.38	18.37	18.51	17.84	18.08	18.62	18.86	18.88	
Cr <sub>2</sub> O <sub>3</sub>	0.03	0.03	0.05	0.1	0	0.08	0	0.03	0	0.07	0.06	0.1	
Fe <sub>2</sub> O <sub>3</sub>	0	0	0	0	0	0	0	0	0	0	0	0	
FeO	16.38	16.58	16.53	17.07	16.3	16.35	16.74	17	17.28	16.62	16.87	16.1	
MnO	0.04	0.03	0.07	0.03	0.02	0	0	0.04	0	0	0	0.03	
MgO	11.73	11.71	11.67	11.93	12.4	11.61	12.15	12.02	11.76	12.1	11.78	11.97	
CaO	0.12	0.19	0.02	0.11	0.04	0.22	0.03	0.05	0	0.04	0.02	0.03	
Na <sub>2</sub> O	0.13	0.11	0.11	0.14	0.17	0.45	0.16	0.19	0.17	0.25	0.16	0.18	
K <sub>2</sub> O	9.48	9.06	9.52	9.36	9.6	9.26	9.49	9.31	9.53	9.39	9.28	9.23	
Total	93.35	93.09	92.46	94.87	94.42	92.3	94.07	94.95	95.32	96.04	95.39	94.97	
Oxygen	11	11	11	11	11	11	11	11	11	11	11	11	
Si	2.735	2.742	2.762	2.771	2.747	2.7	2.726	2.754	2.738	2.73	2.722	2.722	
Ti	0.108	0.115	0.102	0.107	0.069	0.073	0.068	0.11	0.121	0.124	0.113	0.12	
Al	1.622	1.604	1.573	1.562	1.639	1.684	1.661	1.586	1.604	1.631	1.665	1.668	
Cr	0.002	0.002	0.003	0.006	0	0.005	0	0.002	0	0.004	0.004	0.006	
Fe <sup>3+</sup>	0	0	0	0	0	0	0	0	0	0	0	0	
Fe <sup>2+</sup>	1.051	1.066	1.073	1.078	1.031	1.063	1.066	1.072	1.088	1.033	1.056	1.009	
Mn	0.003	0.002	0.005	0.002	0.001	0	0	0.003	0	0	0	0.002	
Mg	1.341	1.341	1.35	1.342	1.398	1.346	1.379	1.351	1.319	1.34	1.315	1.337	
Ca	0.01	0.016	0.002	0.009	0.003	0.018	0.002	0.004	0	0.003	0.002	0.002	
Na	0.019	0.016	0.017	0.02	0.025	0.068	0.024	0.028	0.025	0.036	0.023	0.026	
K	0.928	0.888	0.943	0.902	0.927	0.919	0.922	0.895	0.915	0.89	0.886	0.883	
Sum	7.82	7.793	7.829	7.8	7.841	7.877	7.848	7.804	7.81	7.792	7.786	7.776	
X <sub>Mg</sub>	0.56	0.56	0.56	0.55	0.58	0.56	0.56	0.56	0.55	0.56	0.55	0.57	



**Table 2** (continued)

Min	Bt <sub>4</sub> ^Grt fracture	Bt <sub>4</sub> ^Grt fracture	Kfs <sub>2</sub> M(C)	Kfs <sub>2</sub> M(C)	Kfs <sub>2</sub> M(C)	Pl <sub>2</sub> M(C)	Pl <sub>2</sub> M(C)	Pl <sub>2</sub> M(C)	Pl <sub>2</sub> M(C)	Pl <sub>2</sub> M(C)
SiO <sub>2</sub>	36.35	35.87	63.53	63.86	63.96	60.83	61.46	60.76	61.03	60.84
TiO <sub>2</sub>	0.1	0.59	0.04	0.06	0.07	0.02	0	0.02	0.01	0.06
Al <sub>2</sub> O <sub>3</sub>	18.93	19.57	17.27	17.59	17.79	23.29	23.34	23.12	23.43	23.21
Cr <sub>2</sub> O <sub>3</sub>	0.03	0.01	0.04	0	0.04	0.04	0	0	0	0.03
Fe <sub>2</sub> O <sub>3</sub>	0.91	0.86	0.18	0	0	0.03	0.04	0.06	0.11	0.01
FeO	12.63	14.1	0	0	0	0	0	0	0	0
MnO	0	0	0	0	0	0	0	0	0	0.07
MgO	14.35	13.42	0	0.01	0	0	0	0	0	0.02
CaO	0.04	0.08	0.06	0	0.02	5.82	5.75	5.82	5.93	5.94
Na <sub>2</sub> O	0.16	0.61	1.98	1.79	1.58	8.25	8.23	8.44	8.32	8.21
K <sub>2</sub> O	9.67	8.96	13.69	13.37	13.69	0.19	0.3	0.17	0.18	0.2
Total	93.17	94.08	96.79	96.68	97.15	98.47	99.12	98.39	99.01	98.59
Oxygen	11	11	8	8	8	8	8	8	8	8
Si	2.744	2.695	3.014	3.019	3.013	2.744	2.753	2.746	2.74	2.744
Ti	0.006	0.033	0.001	0.002	0.002	0.001	0	0.001	0	0.002
Al	1.685	1.733	0.966	0.981	0.988	1.239	1.233	1.232	1.24	1.234
Cr	0.002	0.001	0.002	0	0.001	0.001	0	0	0	0.001
Fe <sup>3+</sup>	0.053	0.049	0.006	0	0	0.001	0.001	0.002	0.004	0
Fe <sup>2+</sup>	0.797	0.886	0	0	0	0	0	0	0	0
Mn	0	0	0	0	0	0	0	0	0	0.003
Mg	1.614	1.503	0	0.001	0	0	0	0	0	0.001
Ca	0.003	0.006	0.003	0	0.001	0.281	0.276	0.282	0.285	0.287
Na	0.023	0.089	0.182	0.164	0.144	0.722	0.715	0.74	0.724	0.718
K	0.931	0.859	0.829	0.807	0.823	0.011	0.017	0.01	0.01	0.012
Sum	7.859	7.855	5.004	4.974	4.974	5.001	4.996	5.011	5.005	5.001
X <sub>Mg</sub>	0.67	0.63								
X <sub>An</sub>						0.28	0.27	0.27	0.28	0.28

C core, R rim, I inclusion, M matrix, ^ against; mineral abbreviations are after Kretz (1983)

garnet fractures and boundaries. Similar TiO<sub>2</sub> content (1.77 pfu) noted in one such biotite grains (Table 2) with some of the biotite grains (Bt<sub>3</sub>; 1.74–1.88 pfu) from the S<sub>3</sub> layers indicates that they crystallized at comparable temperatures. Hence, we conclude that retrogression along garnet fractures is at the veining stages of D<sub>2</sub>. The lower TiO<sub>2</sub> (0.1–0.59 pfu) and higher X<sub>Mg</sub> (0.63–0.67) contents in most of the biotite grains seen in garnet fractures compared to the Bt<sub>3</sub> suggest that biotite crystallization continued to lower temperatures after the melt had largely crystallized and solid-state deformation occurred in S<sub>3</sub> fabric.

### Constraints on *P–T* conditions of melting

A key factor in pseudosection analyses is to determine the ‘effective bulk composition’, which represents the equilibration volume of the rock (Spear 1993; Stüwe 1997). This equilibration volume varies from grain scale, e.g., zoned minerals and reaction coronae (Nasipuri et al. 2009) to larger

scales, i.e., in hand specimen scale (Stüwe 2007; Kelsey et al. 2005; Nasipuri et al. 2009). In the studied migmatite sample RAM-1, garnet, biotite, and plagioclase in different layers show strong compositional homogeneity (Table 2). This suggests that the length scale of mineral equilibration attained during metamorphism was larger than the scale of the layers of mineralogical segregations (Fig. 2b, c); the equilibration was possibly aided by element transfer across neosomes of varying width (couple of mm to cm) which are seen to be commonly inter-layered and dispersed in biotite + sillimanite segregations. Consequently, for pseudosection analyses we use the bulk rock composition derived from a hand specimen to define the effective bulk composition (results given in Table 3).

*P–T* pseudosections were constructed (Table 3) in the NCKFMASH system using the PERPLE\_X (Connolly 2005) software built on the thermodynamic database of Holland and Powell (1998) modified in 2004. Manganese was excluded from the system as the spessartine contents in

**Table 3** XRF data of RAM-1

SiO <sub>2</sub>	55.550
Al <sub>2</sub> O <sub>3</sub>	18.780
Fe <sub>2</sub> O <sub>3</sub>	8.860
MnO	0.030
MgO	6.520
CaO	1.250
Na <sub>2</sub> O	1.360
K <sub>2</sub> O	5.240
TiO <sub>2</sub>	0.880
P <sub>2</sub> O <sub>5</sub>	0.070
LOI	1.387
Sum	99.927

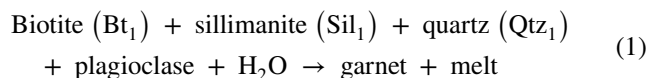
garnet is extremely low, and manganese is absent in other Fe–Mg phases (Table 2). The TiO<sub>2</sub> content in the rock is low and, therefore, also excluded in the computation. Solution models for phases used in *P–T* pseudosection modeling are: (1) garnet: hybrid model of Holland and Powell (1998), Engi and Wersin (1987); (2) biotite: White et al. (2007); (3) muscovite: hybrid model of Coggon and Holland (2002) and Auzanneau et al. (2010); (4) feldspar: Benisek et al. (2004); (5) melt: hybrid model of Holland and Powell (2001) and White et al. (2001).

Melt volume percentages depend on the availability of free H<sub>2</sub>O during initiation and progress of partial melting reactions (Webb et al. 2015). H<sub>2</sub>O influencing partial melting reactions is primarily produced by dehydration reactions in surrounding rocks that may eventually get trapped in the rocks or added to the rock along shear zones (Brown 2002; White and Powell 2002, 2010; Webb et al. 2015). To estimate the H<sub>2</sub>O available in the rock during partial melting under both H<sub>2</sub>O-fluxed and H<sub>2</sub>O-absent conditions, we constructed isobaric T–M<sub>H<sub>2</sub>O</sub> pseudosections (“Appendix” Fig. 11a, b; M<sub>H<sub>2</sub>O</sub> representing mol% of water in the bulk). We chose reference pressures of 6 and 8 kbar based on the 6–8 kbar pressure reported for the Grenvillian-age peak metamorphic condition obtained in mica schists of the Bhilwara Supergroup rocks from the Pur-Banera area (Ojha et al. 2016). The T–M<sub>H<sub>2</sub>O</sub> pseudosections indicate stability of garnet–sillimanite–feldspar (ternary)–quartz–biotite–melt assemblage during H<sub>2</sub>O-deficient melting at temperature ranges of 690–840 °C, and during H<sub>2</sub>O-fluxed melting at 690–750 °C. H<sub>2</sub>O contents for H<sub>2</sub>O-undersaturated and water-fluxed conditions partial melting, as estimated from the T–M<sub>H<sub>2</sub>O</sub> pseudosections have been considered for construction of the *P–T* pseudosections in Fig. 5a–d.

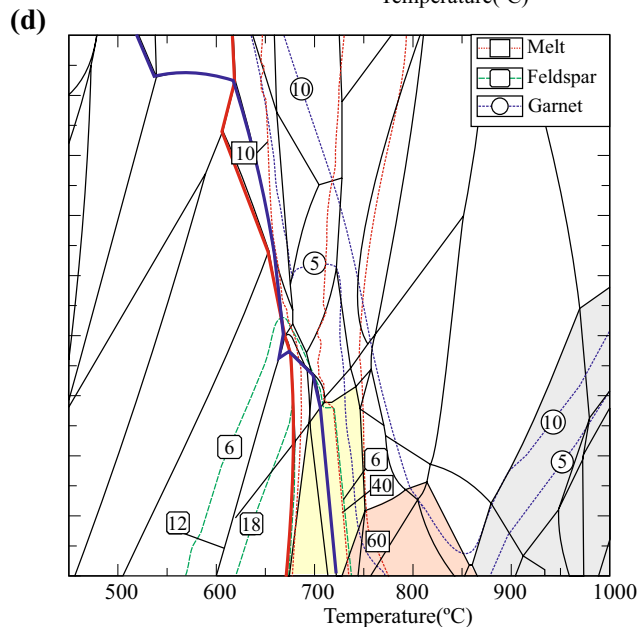
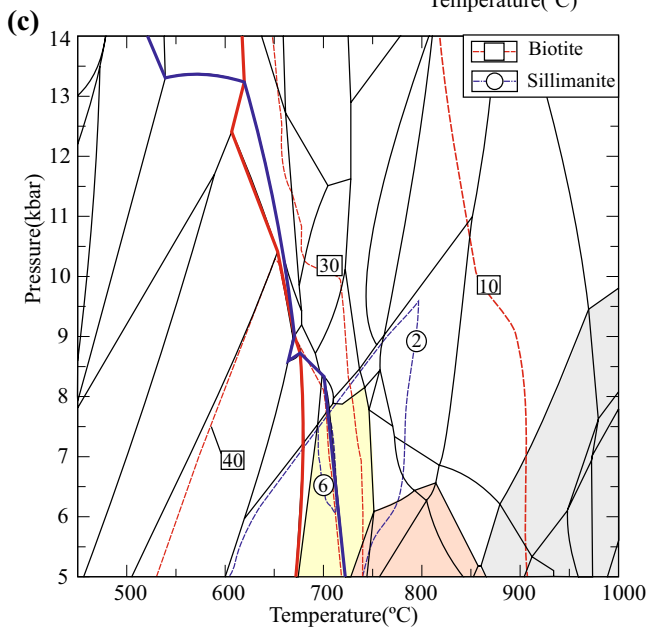
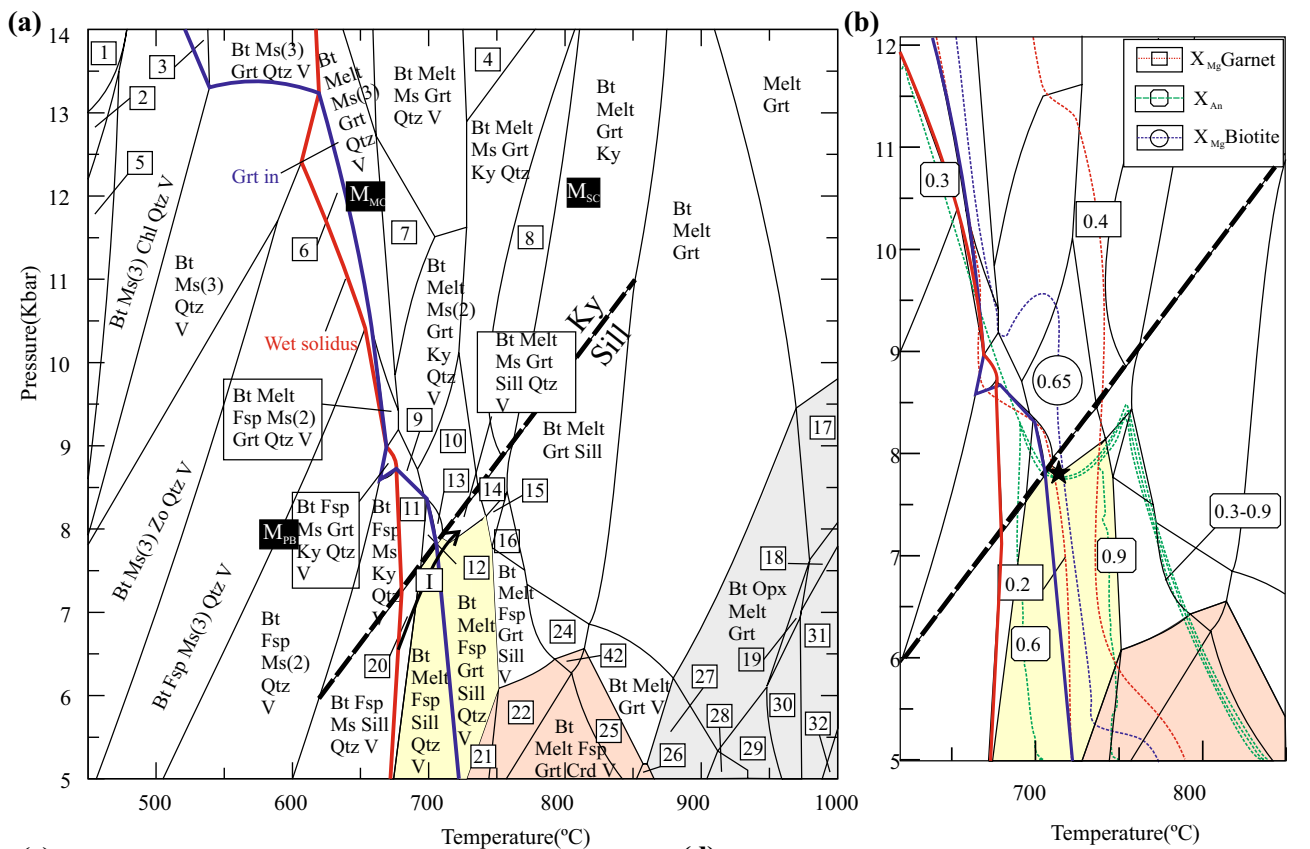
The *P–T* pseudosections show stability of the garnet–sillimanite–feldspar–quartz–biotite–melt peak metamorphic assemblage in *P–T* ranges of 5–8 kbar, 720–740 °C during H<sub>2</sub>O-fluxed melting and ~780–850 °C, 5–10 kbar at

**Fig. 5** Pseudosections in NCKFMASH system from bulk composition of RAM-1. Molar proportions under H<sub>2</sub>O-fluxed conditions are SiO<sub>2</sub>:Al<sub>2</sub>O<sub>3</sub>:FeO:MgO:CaO:Na<sub>2</sub>O:K<sub>2</sub>O: H<sub>2</sub>O=48.33:9.63:5.22:8.48:1.15:1.15:2.90:23.14. **a** *P–T* pseudosection under H<sub>2</sub>O-fluxed melting condition, showing stability field of garnet–sillimanite–feldspar–biotite–quartz–melt-bearing assemblage noted in the sample, at *P–T* ranges of 5–8 kbar, 725–780 °C. **b** Compositional isopleths of garnet, biotite and feldspar in the *P–T* pseudosection of **c** and star sign indicates highest *P–T* for melting reaction. **c, d** Modal isopleths of different phases in the *P–T* pseudosection of **(a)**. **e** *P–T* pseudosection under H<sub>2</sub>O-absent melting condition. Oxide molar proportions of the bulk are SiO<sub>2</sub>:Al<sub>2</sub>O<sub>3</sub>:FeO:MgO: CaO:Na<sub>2</sub>O:K<sub>2</sub>O:H<sub>2</sub>O=58.09:11.57:6.27:10.19:1.38:1.38:3.49:7.62. **f** Compositional isopleths of garnet, biotite and feldspar in the *P–T* pseudosection of **(e)**. The yellow-, gray- and pink-shaded fields, respectively, show stability of biotite ± garnet, orthopyroxene and cordierite with melt. M<sub>MC</sub>, M<sub>SC</sub> and M<sub>PB</sub> show peak *P–T* conditions for the Grenvillian anatexis in the Mangalwar Complex (after Bhowmik et al. 2010), Sandmata Complex (after Saha et al. 2008) and Pur-Banera supracrustals (after Ojha et al. 2016)

H<sub>2</sub>O-absent melting (Fig. 5a, e). In both cases, garnet modal isopleths increase with temperature and increasing melt modes and decreasing biotite and sillimanite modes thus indicating formation of garnet as a peritectic phase (Fig. 5c, d). Within the field of the peak assemblage in the *P–T* pseudosections in Fig. 5b, f, (marked as yellow), the X<sub>Mg</sub> isopleth of 0.2 for peritectic garnet (corresponding to the measured core composition of garnet porphyroblasts, Table 2) is bracketed between 730 °C and 780–800 °C. The computed volume % of melt in equilibrium with garnet compositional isopleth of X<sub>Mg</sub>=0.2, in case of H<sub>2</sub>O-fluxed melting is higher than the melt percolation threshold limit (~10–12 vol%) and lower for H<sub>2</sub>O-absent melting (Fig. 5d, e). Since the sample studied here is a migmatite where melt-rich layers form distinct bands supporting melt migration during formation of peritectic garnet porphyroblasts (Fig. 2a–c), we propose that the partial melting of the rock occurred under H<sub>2</sub>O-fluxed conditions when the mechanical conditions for melt segregation and migration was imparted. Peak pressure for stability of the assemblage garnet–biotite–sillimanite–melt is estimated to be ~8 kbar where the X<sub>Mg</sub> isopleth (0.2) for garnet intersects the muscovite-in line (yellow field) in Fig. 5a, b (for water-fluxed melting). Based on isopleth thermometry from garnet composition, the peak *P–T* estimated is ~8 kbar, 730 °C (Fig. 5b) for the following melting reaction (1):



The reaction is also supported by the textural observations like occurrences of inclusion trails of biotite (Bt<sub>1</sub>) and sillimanite (Sil<sub>1</sub>) in garnet porphyroblasts (Fig. 3a, b). The X<sub>An</sub> isopleth of ~0.3 is the same as that measured in the plagioclase grains (in the leucocratic domains) in textural equilibrium with garnet. This isopleth intersects the garnet



- |                                    |                                |                              |                               |
|------------------------------------|--------------------------------|------------------------------|-------------------------------|
| 1: Bt Ms(2) Ctd Law Chl Qtz V      | 2: Bt Ms(2) Law Chl Qtz V      | 3: Bt Ms(3) Grt Chl Qtz V    | 4: Bt Melt Ms Grt Qtz         |
| 5: Bt Ms(3) Zo Chl Qtz V           | 6: Bt Melt Ms(3) Qtz V         | 7: Bt Melt Ms(2) Grt Qtz V   | 8: Bt Melt Grt Ky Qtz         |
| 9: Bt Melt Fsp Ms Grt Ky Qtz V     | 10: Bt Melt Ms Grt Ky Qtz V    | 11: Bt Melt Fsp Ms Ky Qtz V  | 12: Bt Melt Fsp Ky Qtz V      |
| 13: Bt Melt Fsp Grt Ky Qtz V       | 14: Bt Melt Ms Grt Sill Qtz    | 15: Bt Melt Fsp Grt Sill Qtz | 16: Bt Melt Fsp Grt Sill      |
| 17: Opx Melt Grt                   | 18: Opx Melt Grt Spr           | 19: Bt Opx Melt Grt Spr      | 20: Bt Melt Fsp Ms Sill Qtz V |
| 21: Bt Melt Fsp Grt Sill Crd Qtz V | 22: Bt Melt Fsp Grt Sill Crd V | 23: Bt Melt Grt Sill Crd V   | 24: Bt Melt Grt Sill V        |
| 25: Bt Melt Grt Crd V              | 26: Bt Opx Melt Grt Crd V      | 27: Bt Opx Melt Grt V        | 28: Bt Opx Melt V             |
| 29: Bt Opx Melt                    | 30: Bt Opx Melt Spr            | 31: Opx Melt Spr             | 32: Opx Melt                  |



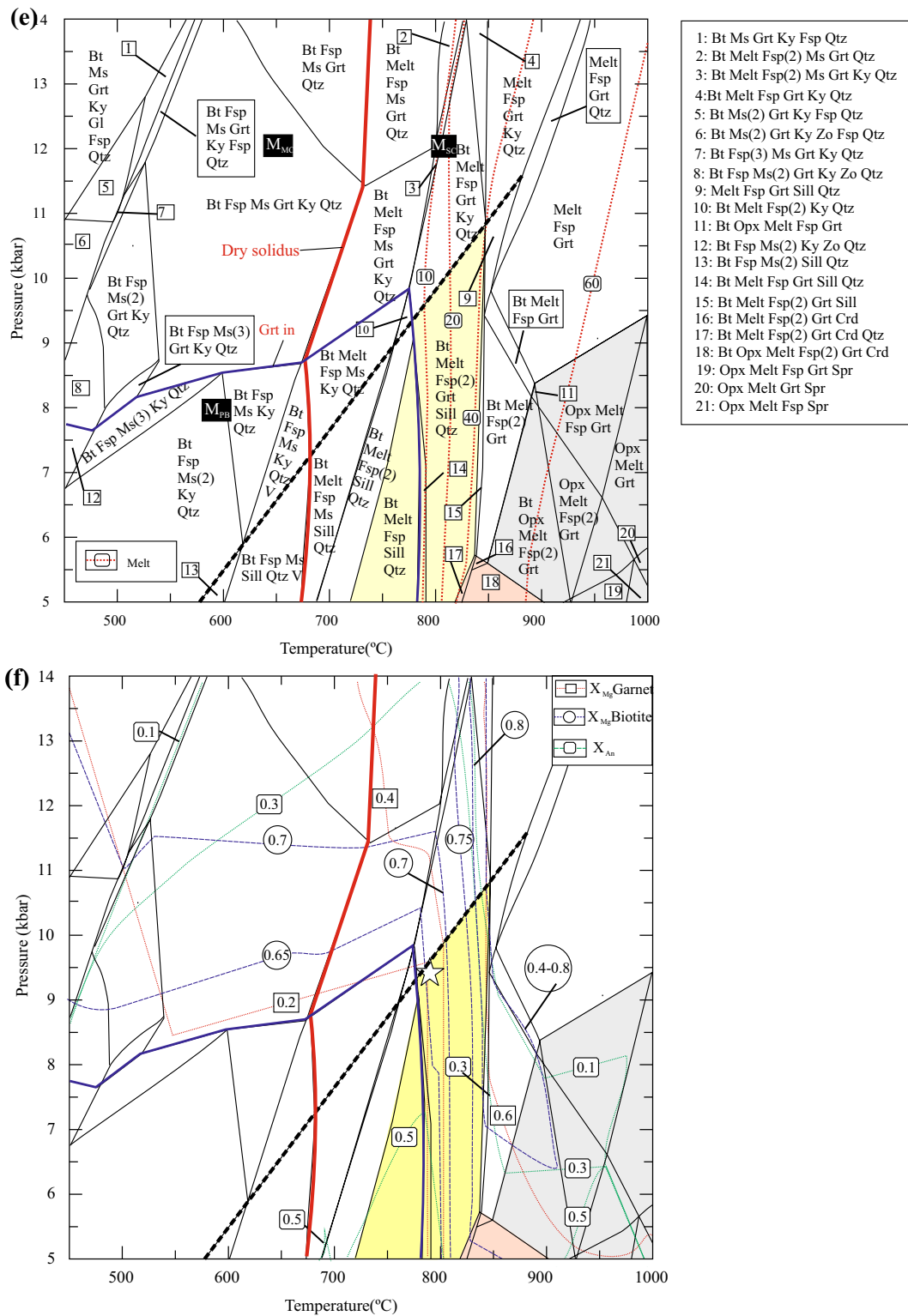


Fig. 5 (continued)

compositional isopleth of  $X_{Mg}=0.2$  at the peak  $P$ - $T$  conditions of  $\sim 8$  kbar,  $730$  °C (Fig. 5b). For conventional thermometry, we have chosen the near-peak pressure of 8 kbar

obtained from isopleths thermobarometry as a reference pressure for calculating temperatures from garnet cores, rims and biotites ( $Bt_2$ ) crystallized in melt-rich domains. Average

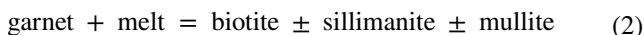
**Table 4** Results of geothermometry

S. no	Grt	Bt	Bh (°C)	Dg (°C)	FS(°C)	H (°C)	HP(°C)	Average Grt-Bt (°C)
At 8 kbar reference pressure								
1	C	Bt <sub>1</sub> ^Grt	630	597	731	708	794	692
2	C	Bt <sub>2</sub> (C)	631	640	706	699	763	688
3	C	Bt <sub>2</sub> (C)	628	632	697	693	760	682
4	C	Bt <sub>2</sub> (C)	626	632	688	692	746	677
5	R ^ Qtz (M)	Bt <sub>2</sub> (C)	617	612	671	680	754	667
At 6 kbar reference pressure								
6	R^Bt <sub>4</sub>	Bt <sub>4</sub>	531	518	515	596	517	535
7	R^Bt <sub>3</sub>	Bt <sub>3</sub> (C)	561	518	564	619	615	576
8	R^Bt <sub>3</sub>	Bt <sub>3</sub> (R^Grt)	556	508	557	609	588	564
9	R^Bt <sub>3</sub>	Bt <sub>3</sub> (C)	547	491	536	597	567	548
10	R^Bt <sub>3</sub>	Bt <sub>3</sub> (C)	570	530	577	620	615	583
11	R^Bt <sub>3</sub>	Bt <sub>3</sub> (C)	563	525	563	613	603	574

Bh Bhattacharya et al. (1992), Dg Dasgupta et al. (1991), FS Ferry and Spear (1978), H Holdaway (2000), HP Holland and Powell (1998), M matrix, I inclusion; C core, R rim

temperature obtained for these pairs is ~680 °C (maximum and minimum values ranging from 670 to 690 °C; Table 4). This temperature is within the temperature range obtained from the garnet core and biotite inclusion data (690 °C). Any prograde path that may be proposed for reaction in Eq. 1 for the studied sample will cross the wet-solidus in the pseudosection, with increase in pressure and temperature (Fig. 5a).

Fractures in garnet porphyroblasts are filled with biotite and/or biotite + sillimanite + mullite (Fig. 3a, c, g). High  $X_{Mg}$  values of biotites in these fractures indicate metamorphic origin rather than crystallization from any melt. So it is proposed that these biotites were formed by back reaction between melt trapped in fractures and garnets during melt-present reaction:



Because of variable equilibration volumes for such reactions which are smaller than even a thin-section scale, their bulk composition cannot be determined and hence the reaction in Eq. 2 could not be modeled by any pseudosection analyses. Nevertheless, it may be predicted that the retrograde segment of any clockwise  $P$ – $T$  path for such orogenic metamorphism will cross the  $H_2O$ -saturated solidus for biotite melting at ~6 kbar (Fig. 10). Hence, we infer that the retrograde section of the clockwise  $P$ – $T$  path corroborates the back reaction between garnet and residual melt, which was  $H_2O$  rich, leading to the formation of the retrograde  $Bt_4 \pm Sil_4 \pm Mul_4$  assemblage. For calculating the retrograde temperature range we have chosen the reference pressure at 6 kbar, which is the minimum pressure obtained for the retrograde section of  $P$ – $T$  path in Fig. 10. At this reference pressure, rims of garnet against

the adjoining biotites ( $Bt_3$ ) in the  $S_3$  fabric yield average temperature of ~570 °C (maximum and minimum temperatures being 550–580 °C, Table 4); this estimate is somewhat higher than what is inferred from the compositions of garnet and biotite ( $Bt_4$ ) lodged in the garnet fracture (~540 °C). Hence, we infer that on the retrograde section of the clockwise  $P$ – $T$  path a back-reaction between garnet and residual melt occurs.

### Crystallographic and microstructural characterization

To constrain deformation mechanisms of the phases in the presence of melt detailed crystallographic and microstructural analyses were carried out on garnet, quartz and mullite occurring within the different microstructural domains of the migmatite (Fig. 3a).

### General orientation characteristics of mullite, quartz and garnet

**Mullite** Mullite ( $Mul_1$ ) occurring along the two limbs of  $D_1$  micro-folds hosted within  $D_2$  garnet porphyroblasts shows contrasting orientations (Fig. 6a, b). Elongate mullite mats ( $Mul_3$ ) defining the  $S_3$  foliation in the matrix show a strong CPO, with the  $c$  axes parallel to the stretching lineation ( $X$  direction) and (010) plane perpendicular to the foliation plane (Fig. 6c, d).

**Quartz** Quartz occurs in different textural domains (Table 1; Fig. 4). Quartz grains at the hinges of  $D_1$  rootless fold in the matrix ( $Qtz_1$ ; Fig. 7a, b) exhibit a high number of subgrains and dauphine twins (60° rotation around

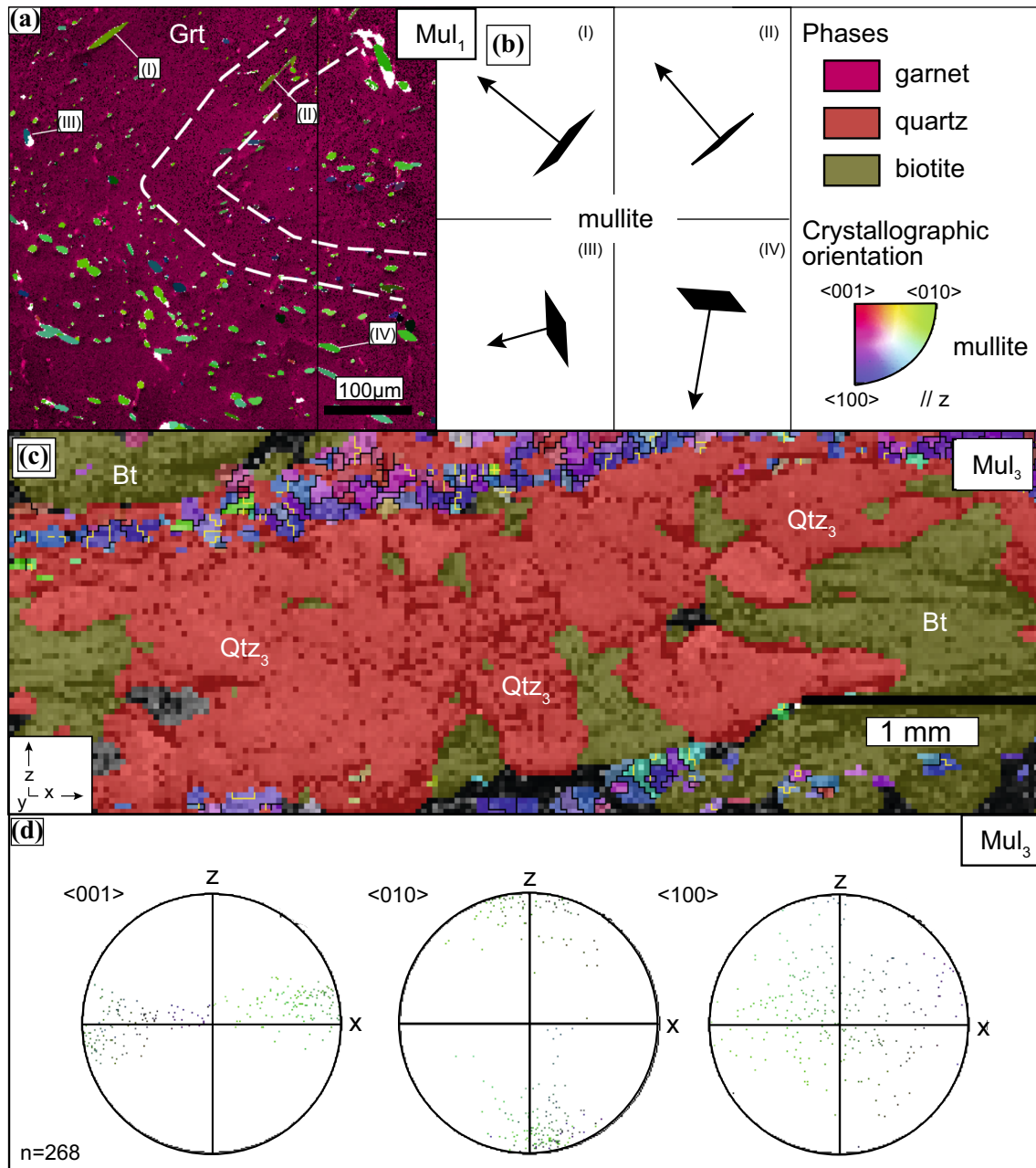


**Fig. 6** Orientation characteristics of different mullite types **a**  $Mul_1$ ; orientation map of garnet grain (lilac) and mullite as inclusions in the grain; note hinge trace (dashed white lines); **b** 3D representation of mullite crystal orientation grains present as inclusion in garnet forming crenulation hinges shown in (a). **c** Orientation map of mullite

$Mul_3$  intergrown with fine-grained biotite (khaki) and fine-grained quartz (red), for mullite coloring signifies crystal orientations as shown in inset. **d** Pole figures showing the orientation of  $Mul_3$  mullite grains shown in (c); one point per grain

*c*-axis) and a distinct CPO with clustering of (0001) poles to plane (Fig. 7c). In contrast, quartz grains within leucocratic layers and intergrown with garnet ( $Qtz_2$ ; Fig. 7b, d) show very weak to random CPO (Fig. 7e). The orientation map of the coarse quartz grains ( $Qtz_2$ ) within  $S_2$  leucosomes in the interfolial domains of  $S_3$  is shown in Fig. 7f. Here, quartz grains exhibit lattice distortions, few continuous

subgrain boundaries and a near-random CPO (Fig. 7g). In contrast, a weak, but distinct CPO (Fig. 7i) is documented in fine-grained quartz ( $Qtz_3$ ) in the biotite–mullite–sillimanite ( $Bt_3$ – $Mul_3$ – $Sil_3$ )-dominated  $S_3$  foliation (Figs. 3a, 7 h, 10).

**Garnet** All analyzed garnet grains exhibit an elongate shape (e.g., Fig. 8a, b, d). All grains have very similar crystallographic orientations (Fig. 8e) even if these grains do

not appear to be physically continuous in the plane of observation (Fig. 3a). The crystallographic orientation map of a representative elongate garnet grain from the  $S_2$  melanocratic band shows an absence of distinct subgrain boundaries and/or systematic crystal lattice bending. However, distinct changes in orientation are seen associated with fractures filled or not filled by quartz, biotite and mullite ( $Mul_3$ – $Bt_3$ ) (Fig. 8b, c, d). Analysis of other garnet grains shows the same absence of systematic crystal lattice distortion or subgrain boundaries.

### Monazite dating

Monazites in the sample occur as inclusions in garnet, quartz ( $Qtz_2$ ) and potash feldspar ( $Kfs_2$ ) in the  $S_2$  layer, and overgrowing  $D_1$  crenulation hinges (Fig. 9a–d). Monazite grains are often anhedral and vary in size from 40 to 100  $\mu m$  (Fig. 9c–o). BSE images show that the monazite grains are mostly homogeneous in composition with some grains having yttrium-rich cores. Monazites included in garnet and potash feldspar ( $Kfs_2$ ) yield 1028 Ma and 920–912 Ma, respectively (Fig. 9a, d, g, k). Cores of monazites occurring within  $S_2$  melt-bearing layer yield ages ranging from 1037 to 930 Ma and ages recorded from their rims vary from 887 to 840 Ma (Fig. 9e, f, h, n; Table 5). Monazites from the  $S_3$  foliations yield 965–889 Ma from the cores and 887–850 Ma from their rims (Fig. 9i, l–m, o; Table 5). The 33 monazite spot ages obtained from 15 grains yield two unmixed populations:  $914 \pm 11$  Ma and  $1285 \pm 64$  Ma (Fig. 9r). The older age population ( $\sim 1285$  Ma) is obtained from the core of one monazite included in a garnet porphyroblast.

## Discussion

### Conditions of migmatization and synchronous deformation

Field and microscopic observations indicate that melting in the garnet–sillimanite migmatites of Rampura–Agucha initiated post- $D_1$ , and was pronounced during the  $D_2$  deformation stage resulting in melt segregation and formation of  $S_2$  layering including coarse-grained leucocratic, garnet-bearing bands and fine-grained, restitic layers dominated by biotite, mullite and some quartz. The absence of melts cross-cutting  $D_3$  fabrics precludes anatexis during or after the  $D_3$  deformation.

Microstructural observations (Fig. 3a, b) and pseudo-section analyses indicate that the  $D_2$  peritectic garnet was formed during a  $H_2O$ -fluxed partial melting event at the expense of  $D_1$  biotite–sillimanite aggregates at  $\sim 725$  °C and at pressure  $\sim 8$  kbar under granulite facies conditions

indicated by isopleth thermometry involving garnet compositions (Figs. 5b, 10). The temperature recorded is thus close to the biotite melting reaction temperatures determined from pseudo-section modeling using average metapelite bulk composition (White et al. 2001; Saha et al. 2008). A tight-loop clockwise  $P$ – $T$  path constructed for the metamorphic event (Fig. 10) indicates rapid burial and exhumation. Since the garnet porphyroblasts are chemically homogeneous, it is suggested that high degree of chemical equilibrium was attained at the anatexis conditions as ubiquitous melt allowed rapid elemental exchange. Biotite and/or sillimanite in the fractures of garnet porphyroblasts were formed by back-reactions with the melts trapped in the fractures during late stages of partial melt crystallization which marks the onset of retrogression (Figs. 3c, 10).

### The Aravalli–Delhi Fold Belt represents part of the Grenvillian-age orogeny in Northern India

Enclaves of polycyclic granulite facies migmatites from the Sandmata Complex of BGC-II (Fig. 1b) occur within charnockitic gneisses (Saha et al. 2008; Bhowmik et al. 2010). These migmatite enclaves record two partial melting events, namely  $M_1$  at  $\sim 1.7$ – $1.6$  Ga in the sillimanite stability field, at 6–7 kbar and 850 °C, followed by a second event ( $M_2$ ) at  $\sim 1.0$  Ga in kyanite stability field, at  $\sim 14$  kbar, 850 °C (Fig. 5a, e; Saha et al. 2008). The high-pressure Grenvillian-age  $M_2$  partial melting event recorded in the enclaves has also been recorded from the host felsic gneisses. Based on zircon and monazite ages from the gneisses of the Sandmata Complex and Mangalwar Complex (Fig. 1b), Buick et al. (2006, 2010) proposed recycling of Paleo-Mesoproterozoic ( $\sim 1.7$ – $1.4$  Ga) crustal components during the Grenvillian Delhi orogeny. Bhowmik et al. (2010) reported partial melting of gneisses from the Mangalwar Complex at  $\sim 12$  kbar, 800 °C during the Grenvillian orogeny (Fig. 5a, e). In contrast, for the Grenvillian metamorphism from the Pur-Banera supracrustal sequence (Fig. 1b), Ojha et al. (2016) recorded peak  $P$ – $T$  conditions of  $\sim 8$  kbar, 600 °C (Fig. 5a, e).

In our sample, monazite aligned parallel to the  $S_2$  and  $S_3$  fabrics yield ages ranging between 1000 and 900 Ma (Fig. 9). Similar ages were also recorded by monazite grains sequestered within  $D_2$  garnets suggesting an anatexis event at that time. Rims of monazites in the melt-rich layers yield spot ages of  $\sim 870$ – $850$  Ma, which may be interpreted as minimum age of melting and/or the age range of melt crystallization. Monazite yielding older ages of  $\sim 1286$  Ma (Fig. 9) may be detrital.

In summary, the Rampura–Agucha metapelite migmatites underwent Grenvillian-age anatexis at  $\sim 8$  kbar and 730 °C. Peak  $P$ – $T$  condition was thus at substantially lower pressures than those recorded westwards in the Sandmata Complex.



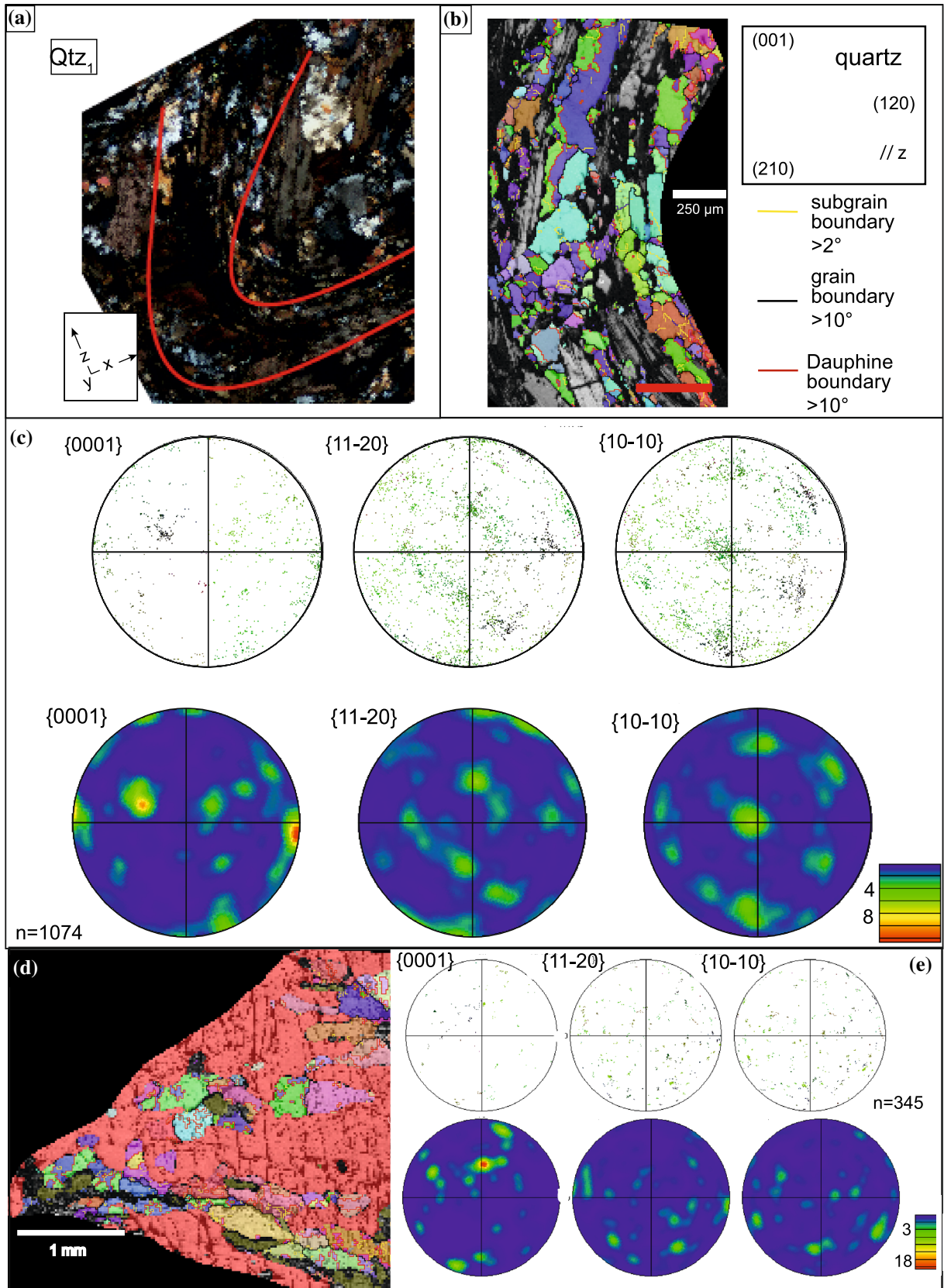




**Fig. 7** Orientation characteristics of different quartz types. **a** Petrographic image of microfold made up by Qtz<sub>1</sub>. **b** Orientation map of microfold limb shown in (a). **c** Pole figures of Qtz<sub>1</sub> corresponding to orientation map of microfold shown in (a, b). **d** Orientation map of Qtz<sub>2</sub> (quartz intergrown with garnet porphyroblast); note the presence of Dauphine twins (red lines) but the absence of subgrain boundaries (yellow lines). **e** Pole figures and contour maps of quartz corresponding to orientation map (d). **f** Orientation map of Qtz<sub>2</sub> coarse-grained quartz from the leucocratic layers of S<sub>2</sub>. **g** Pole figures and contour maps of coarse-grained quartz corresponding to orientation map (f). **h** Orientation map of fine-grained quartz, Qtz<sub>3</sub> intergrown with mullite (Mul<sub>3</sub>) in the S<sub>3</sub> foliation planes. **i** Pole figures and contour maps of fine-grained quartz corresponding to orientation map (h)

### Evolution of deformation microstructures in the Rampura–Agucha migmatite: characteristics and rheological implications

The correlation of microstructural development with the  $P$ – $T$  path vector is given in Fig. 10. Contrasting orientations of mullite (Mul<sub>1</sub>) grains in the limbs of the micro-folds hosted within garnet porphyroblast are consistent with systematic re-orientation (by rigid body rotation) of initially highly aligned mullite grains that inherited strong crystallographic preferred orientation during growth syn-tectonic with D<sub>1</sub>

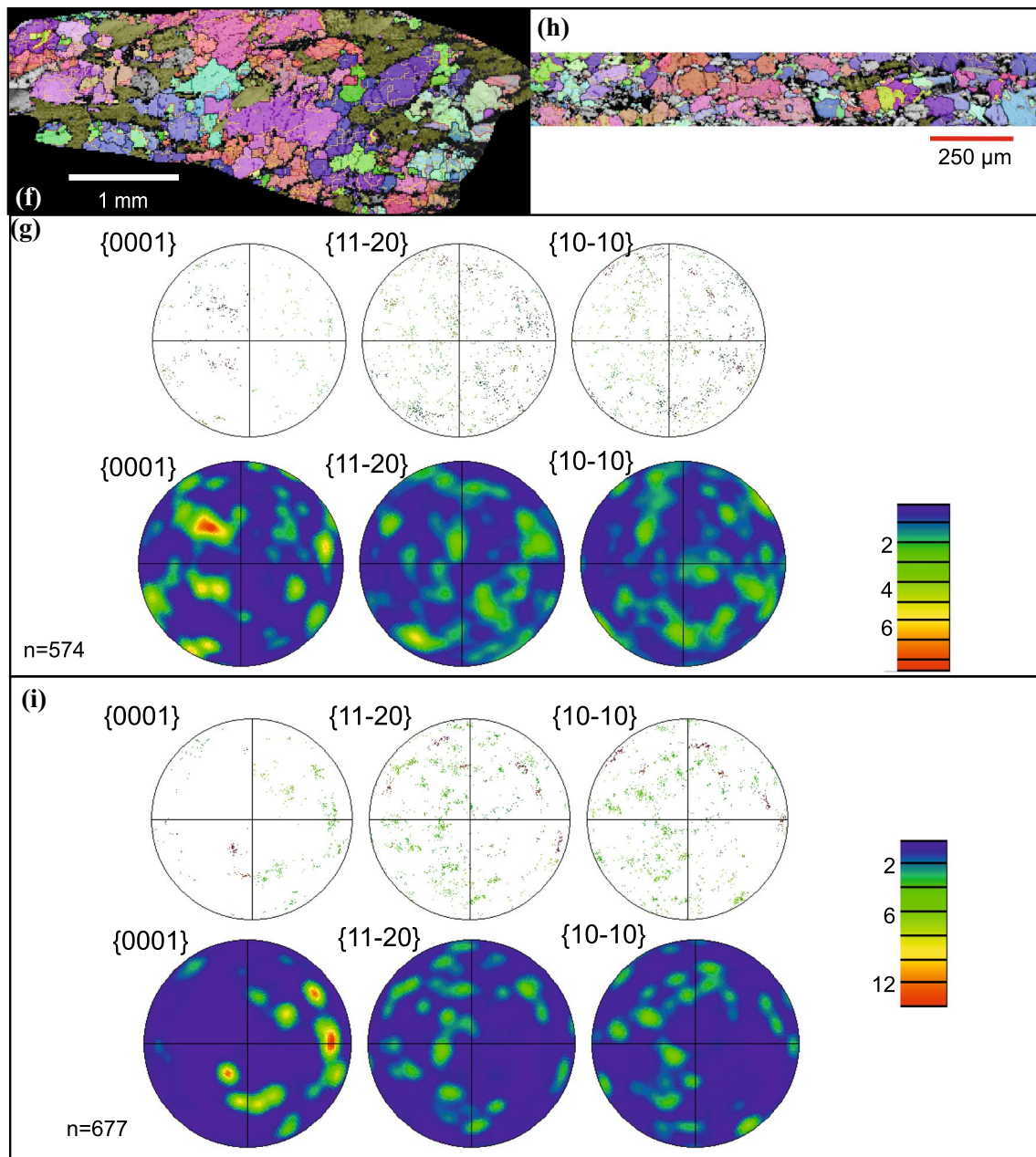


**Fig. 7** (continued)

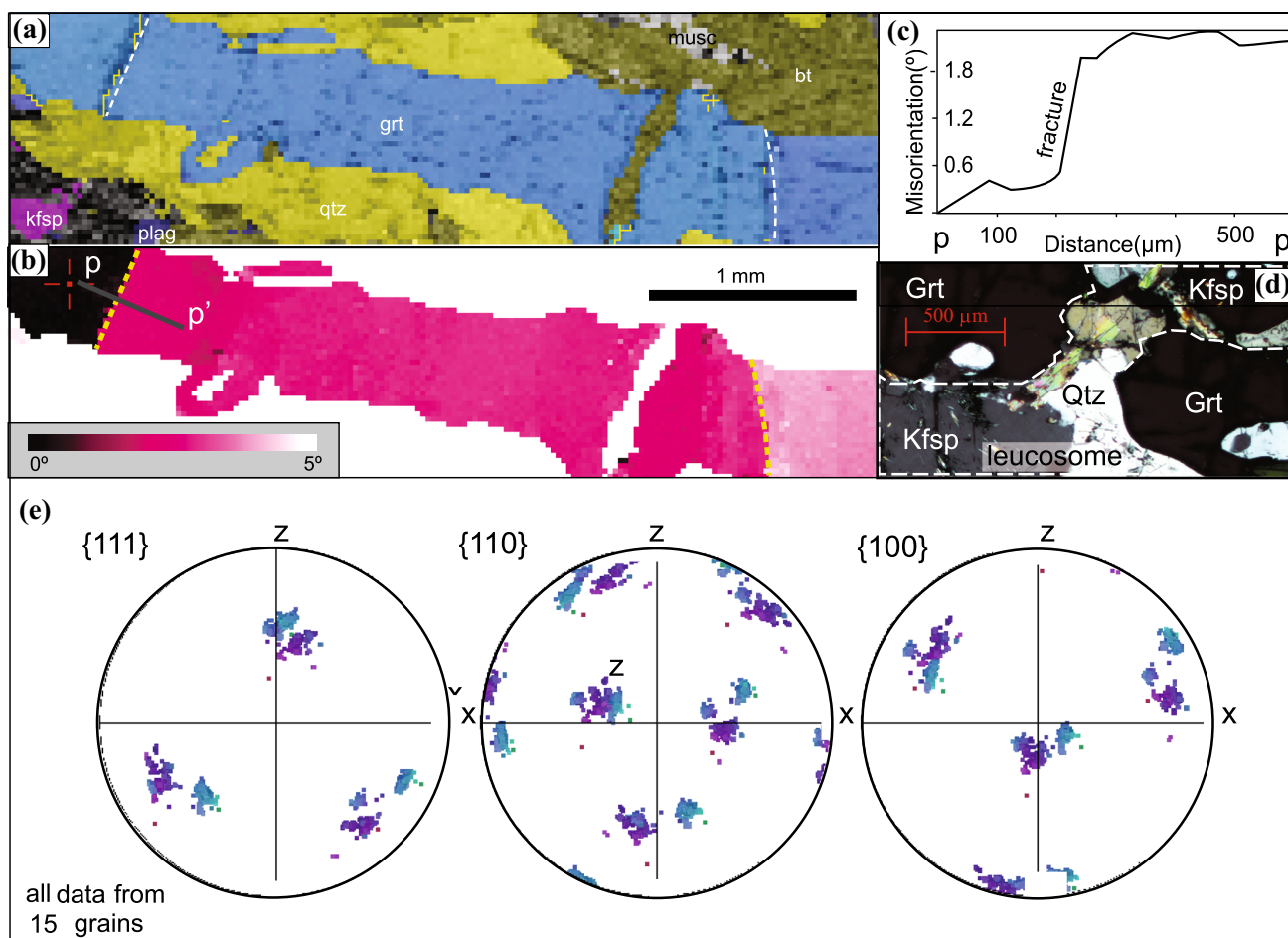


**Fig. 8** Orientation characteristics of garnet grains. **a** Map of elongate garnet grain with surrounding minerals; different phases are shown in different colors; **b** Map of orientation variations within garnet grain shown in (a), color variations indicate the progressive internal misorientation  $0^{\circ}$ – $2^{\circ}$ .  $p$ – $p'$  outline misorientation profile shown in (c); note

in (a) and (b) location of fractures is shown as stippled lines (c). Misorientation profile within grain along line  $p$ – $p'$  shown in (b). **d** Photomicrograph of fracture within elongate garnet porphyroblast; **e** pole figures showing the orientation of all garnet grains by plotting data from 15 different garnet grains; note the similarity in orientation

prior to melting. Solid-state, prograde high strain is manifested by coarse quartz grains ( $Qtz_1$ ) with undulose extinction and subgrains (Fig. 3h, i). EBSD analyses of these quartz grains ( $Qtz_1$ ) in the relict  $D_1$  crenulation hinge in the matrix show a distinct CPO (Fig. 7a–c). The orientation of the  $c$ -axis relative to the reference frame along with the presence of undulatory extinction and distinct subgrains with continuous systematic subgrain boundaries suggests solid-state deformation via dislocation creep. The patterns observed in the pole figure is consistent with a dominance of  $\langle c \rangle$  slip suggesting high- $T$  (650–700 °C) deformation during  $D_1$  (Blumenfeld et al. 1986, Passchier and Trouw 2005; Law 2014; Fig. 7b).

Quartz grains in the leucocratic  $S_2$  domains in the migmatite are coarser than 200  $\mu\text{m}$  and exhibit a very weak to random CPO. Interestingly, despite near absence of a CPO, internally the grains show weak undulatory extinction, and few, discontinuous subgrain boundaries (Fig. 7f, g). We interpret these features to originate from the local stresses

that occur when a melt cools and quartz crystallizes and grows as one of the last phases. During this phase, minor solid-state crystal plastic deformation can be induced, resulting in the observed internal deformation features, but since deformation is not due to regional differential stress, no distinct CPO develops. Similar features have been described by Hasalová et al. (2011) in frozen-in partial melts. We suggest that the newly crystallized coarse quartz grains escaped deformation post-anatexis because as the melt pool solidified, strain was partitioned first into adjacent melt-bearing rheologically weak domains; hence, the solidified melt pool deformed only to a minor extent. Once, all melt had solidified these coarse-grained domains were not subjected to the significant solid-state deformation. This lack of crystal plastic deformation imposed during later retrograde deformation is similar to conclusions for similar migmatitic rocks (Hasalová et al. 2011; Menegon et al. 2011).



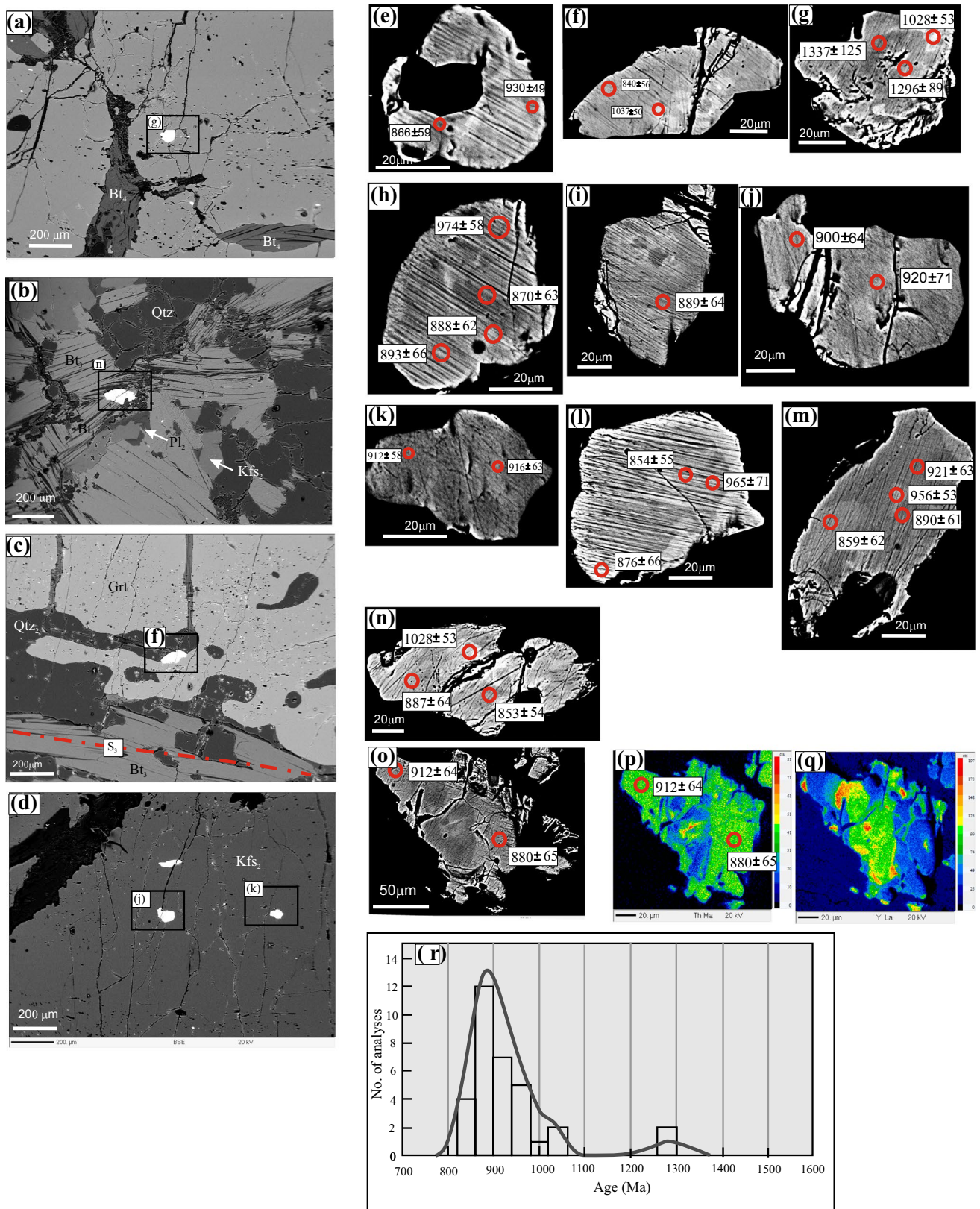


**Fig. 9** Microstructural relationships (BSE images) of the monazites (a–d), BSE images of monazite grains with spot ages (e–o), X-Ray Th and Y images of monazite grains (p–q) and probability density plot of monazite grains from the sample RAM-1

**Table 5** Analytical data (EPMA) for the dated monazites of sample RAM-1

	Texture	Pb	Th	U	Age (Ma)	2 sigma	%Error
1	Contact of Qtz <sub>2</sub> in S <sub>2</sub>	0.54	10.01	0.83	930	49	5.27
2	Contact of Qtz <sub>2</sub> in S <sub>2</sub>	0.36	4.8	1.31	866	59	6.81
3	Contact of garnet and Qtz <sub>2</sub> in S <sub>2</sub>	0.37	4.77	1.46	840	56	6.67
4	Contact of garnet and Qtz <sub>2</sub> in S <sub>2</sub>	0.62	10.28	0.82	1037	50	4.82
5	Contact of Qtz <sub>3</sub> in S <sub>3</sub>	0.33	4.76	1.11	870	63	7.24
6	Contact of Qtz <sub>3</sub> in S <sub>3</sub>	0.44	6.89	0.93	974	58	5.95
7	Contact of Qtz <sub>3</sub> in S <sub>3</sub>	0.32	5.12	0.82	893	66	7.39
8	Contact of Qtz <sub>3</sub> in S <sub>3</sub>	0.35	5.28	1	888	62	6.98
9	Inclusion in Kfs <sub>2</sub> in S <sub>2</sub>	0.31	5.43	0.58	920	71	7.72
10	Inclusion in Kfs <sub>2</sub> in S <sub>2</sub>	0.34	5.12	0.98	900	64	7.11
11	Inclusion in Kfs <sub>2</sub> in S <sub>2</sub>	0.36	6	0.75	916	63	6.88
12	Inclusion in Kfs <sub>2</sub> in S <sub>2</sub>	0.4	5.02	1.36	912	58	6.36
13	Overgrowing Bt <sub>3</sub> in S <sub>3</sub>	0.33	5.41	0.85	889	64	7.20
14	Contact of Qtz <sub>3</sub> in S <sub>3</sub>	0.31	4.83	0.62	991	76	7.67
15	Contact of Qtz <sub>3</sub> in S <sub>3</sub>	0.33	4.67	0.84	965	71	7.36
16	Contact of Qtz <sub>3</sub> in S <sub>3</sub>	0.31	5.11	0.81	876	66	7.53
17	Contact of Qtz <sub>3</sub> in S <sub>3</sub>	0.39	4.95	1.5	854	55	6.44
18	Contact of garnet and Qtz <sub>2</sub> in S <sub>2</sub>	0.36	4.62	1.31	867	60	6.92
19	Inclusion in Grt in S <sub>2</sub>	0.37	5.84	0.98	896	59	6.58
20	Overgrowing Bt <sub>3</sub> in S <sub>3</sub>	0.33	5.26	0.96	859	62	7.22
21	Overgrowing Bt <sub>3</sub> in S <sub>3</sub>	0.36	4.31	1.25	921	63	6.84
22	Overgrowing Bt <sub>3</sub> in S <sub>3</sub>	0.49	8.07	0.92	956	53	5.54
23	Overgrowing Bt <sub>3</sub> in S <sub>3</sub>	0.35	4.57	1.21	890	61	6.85
24	Contact of Qtz <sub>3</sub> in S <sub>3</sub>	0.37	4.85	1.34	883	59	6.68
25	Contact of Qtz <sub>2</sub> in S <sub>2</sub>	0.31	4.43	0.75	963	74	7.68
26	Overgrowing Bt <sub>3</sub> in S <sub>3</sub>	0.33	5.25	0.88	887	64	7.22
27	Overgrowing Bt <sub>3</sub> in S <sub>3</sub>	0.55	9.51	0.65	1028	53	5.16
28	Overgrowing Bt <sub>3</sub> in S <sub>3</sub>	0.4	4.72	1.66	853	54	6.33
29	Contact of garnet and Qtz <sub>2</sub> in S <sub>2</sub>	0.36	3.15	0.84	1273	92	7.23
30	Inclusion in Grt in S <sub>2</sub>	0.51	9.34	0.71	954	52	5.45
31	Inclusion in Grt in S <sub>2</sub>	0.39	5.05	0.41	1296	89	6.87
32	Contact of Qtz <sub>2</sub> in S <sub>2</sub>	0.32	5.2	0.82	880	65	7.39
33	Contact of Qtz <sub>2</sub> in S <sub>2</sub>	0.35	5.26	0.92	912	64	7.02

In contrast, in the S<sub>3</sub> realms the polygonised, finer grained quartz aggregate (10–50 µm; Figs. 7h, 10) shows a weak CPO (Fig. 7i). These aggregates are interleaved with relict prograde biotite, sillimanite and mullite layers that anastomose around the coarser grained domains. The relict nature of the latter phases is inferred from the chemistry of the biotites and is, therefore, also interpreted to represent the restitic parts of a migmatite. Based on to the geometric warping around the coarse-grained garnet-bearing leucosome, these fine-grained, phase-mixed layers must have deformed post-migmatization accommodating strain during the retrograde path. We suggest that deformation occurred during solid state where most of the strain was taken up by the basal slip of biotite along with rigid body rotation of biotite and mullite. Quartz is mostly “passive” as the rheologically weaker biotite and mullite concentrate strain. Therefore, quartz exhibits only minor internal lattice distortions and a weak CPO (Fig. 7i).

We prefer this interpretation to the possibility of dislocation glide accommodated grain boundary sliding at high temperature (> 700 °C), aided by small grain sizes and possibly melt presence at grain boundaries (Schmid 1982; Behrmann and Mainprice 1987; Brodie and Rutter 2000; Song and Ree 2007; Kilian et al. 2011; Svahnberg and Piazzolo 2010). Our preference is based on the fact, that biotite is known to be weak and in mixed, multiphase layers a weak CPO is possible to develop in the “harder” mineral phase. This is due to pronounced strain partitioning between easily deformed phases, e.g., graphite or biotite and a phase requiring higher critical resolved shear stress for activation of slip systems, e.g., ice or quartz (Cyprych et al. 2016). Furthermore, microstructurally there are no indications for melt film presence during D<sub>3</sub> deformation. A consequence of our interpretation is that at the time of the last deformation event, the rock was relatively weak, not due to the presence of

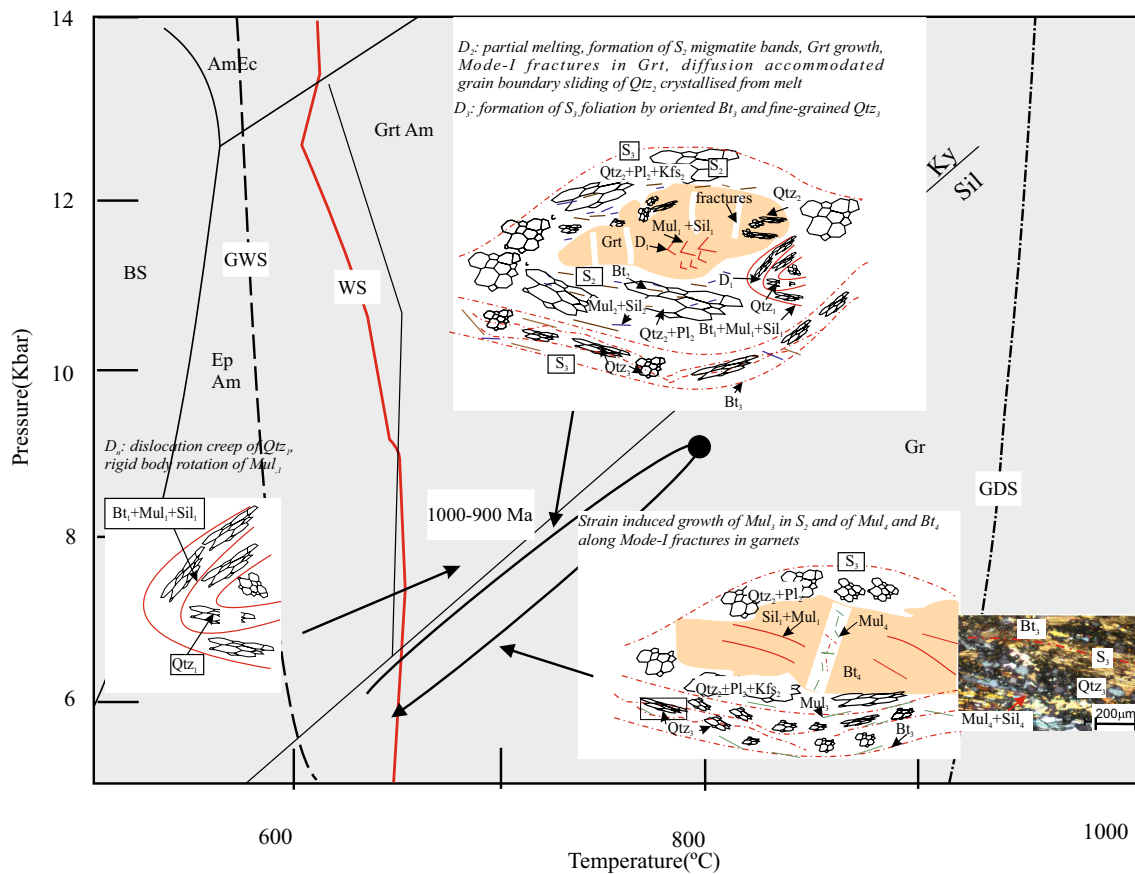


**Fig. 10** Summary of the  $P$ – $T$  path inferred for the migmatite of Bilwara Supergroup from the study area. Also shown are the calculated wet solidus (WSS) from Fig. 5a, granite wet solidus (GWS), granite dry solidus (GDS) curves (after Brown 2002). Schematic drawings show typical microstructures developed at the different segments of  $P$ – $T$  path. Labeling of deformation  $D_1$  to  $D_3$  according to discussion

melt, but due to the presence of fine-grained phase-mixed layers that developed during the transient migmatization event. These fine-grained, biotite- and mullite-rich layers deform at relatively low stresses as suggested by experiments (e.g., of an analogous system of ice and graphite; Cyprych et al. 2016), hence are weak.

In summary, we interpret that high-strain deformation prevailed postdating anatexis. Strain was accommodated by solid-state deformation ( $D_3$ ) within the fine-grained quartz aggregates interleaved with biotite aggregates forming rheologically weak layers, and not by the coarse-grained leucosome domains similar to strain partitioning seen in other layered metamorphic rocks (e.g., Smith et al. 2015).

Large elongate garnet porphyroblasts described here seem at first sight to be similar to those noted by several researchers in metamorphic rocks formed under granulite facies to eclogite facies conditions (Ji and Martignole 1994; Prior et al. 2000; Kleinschrodt and McGrew 2000; Ji et al. 2003; Mainprice et al. 2004; Storey and Prior 2005). These studies

in text, in italic deformation mechanisms for noted minerals. This section photograph shows presence of polygonal fine-grained quartz from  $S_3$  layers (marked with the box). See text for details. Abbreviations used for metamorphic facies fields are: *BS* blueschist, *AmEc* amphibole eclogite, *EpAm* epidote amphibole, *GrtAm* garnet amphibolite, *Gr* granulite

conclude that under both subsolidus and supra-solidus conditions at different crustal depths coarse garnet crystals may achieve their elongated shape due to crystal–plastic deformation manifested by clear subgrain boundaries and systematic lattice bending. In contrast, the elongate garnet in our sample is characterized by the absence of subgrain boundaries and/or crystal lattice bending (Fig. 8a, b). The occurrence of vermicular quartz intergrown with garnet (Fig. 3b), melt films at feldspar–garnet interfaces (Fig. 3e, f), and melt-bearing domains trapped within garnets (Figs. 8d, 10), unmistakably point to the presence of melt during garnet growth. Furthermore, small plagioclase grains with low dihedral angles possibly represent melt pseudomorphs (Fig. 3j, e.g., Sawyer 2001). Hence, garnet is peritectic growing in response to incongruent melting of biotite–sillimanite aggregates. The extensional Mode I fractures in the elongate garnet porphyroblasts may have been induced by a combination of high fluid/melt pressure exerted by partial melt crystallization (Abe and Urai 2012; Komoróczy et al. 2013; Rimsa et al. 2007; Tretiakova et al. 2016) as well



as tectonic forces (Abe and Urai 2012; Komoróczy et al. 2013). Subsequent to garnet fracturing, growth of biotite and mullite (Bt<sub>4</sub>–Mul<sub>4</sub>) along fractures and along garnet margins (Fig. 3a, g) indicate that melt-rich domains remained in contact with the garnet-bearing layers to promote their growth during cooling and back-reaction. However, these domains remained shielded during subsequent solid-state deformation as garnet and surrounding coarse-grained quartz and orthoclase remained rigid at the D<sub>3</sub> event.

We attribute the elongate shape of garnet to its growth via partial melting (reaction 1) pseudomorphing a pre-existing three-dimensional network of biotite–sillimanite/mullite clusters. Such a biotite–sillimanite network intergrowth explains the uniform crystallographic orientation of garnet as one large garnet grew within the three-dimensional network. We, however, concede that the statistics for making the inference is low (number of grains exposed at the surface of the thin section analyzed = 15).

Mullite stable in the S<sub>3</sub> foliation domains shows no substructure but strong CPOs (Fig. 6c, d), indicating either rigid body rotation in the presence of high shear stress under solid state (see Piazzolo and Jaconelli 2013) or possibly by epitaxial replacements of Kfs<sub>2</sub> in the presence of differential stress-inducing oriented growth during the same late-stage solid-state deformation.

## Conclusions

Our analyses of microstructural development in the garnet–sillimanite–mullite–quartz–feldspar–biotite migmatite in the high-grade Aravalli–Delhi Fold Belt help to identify the supra-solidus to subsolidus deformation mechanisms in a migmatite-preserving signature of its prograde, peak and retrograde pressure–temperature–deformation path experienced by the migmatite. The following conclusions can be drawn.

During the Grenvillian Delhi Orogeny (spanning from 1000–870 Ma), garnet–biotite–sillimanite–mullite–quartz–feldspar-bearing migmatite from the shear zone in the Rampura–Agucha area of Aravalli–Delhi Fold Belt underwent crustal anatexis at ~8–9 kbar, 730 °C which is at much lower depth (~30 km) compared to the high-pressure crustal anatexis of the migmatites from the SC and MC (~14 kbar, >40 km) in the west (Fig. 1). Three main stages of fabric development (S<sub>1</sub>–S<sub>3</sub>) occurred in the rock during the orogeny, where the S<sub>2</sub> metatexite layers were formed on its prograde path which underwent folding leading to formation of biotite–sillimanite–mullite–quartz-bearing axial planar foliations (S<sub>3</sub>). During peak conditions, anatectic incongruent melting reaction involved breakdown of biotite, sillimanite and formation of garnet-bearing peritectic assemblage along a tight loop clockwise *P–T* path. The preservation of sillimanite–mullite–biotite–quartz-bearing inclusion trails in

the Grenvillian-age garnet porphyroblasts and strong CPOs, undulose extinction and subgrain boundaries in quartz grains in the relict crenulation hinges in matrix and within garnets imply that the rock was subjected to a pre-Grenvillian solid-state, high-temperature–deformation event (>650–700 °C).

Peritectic garnet porphyroblasts are elongated with aspect ratios varying from 3.1 to 1.7 with Mode I fractures perpendicular to the elongation. Presence of biotite–sillimanite–mullite in these fractures indicate their crystallization during back-reaction of garnet and trapped hydrous melt during cooling. Absence of subgrain boundaries and systematic crystal lattice bending in the garnet porphyroblasts indicate that their elongated nature is not a result of ductile deformation. We suggest that the garnet grains attained elongated shape as a result of their growth over a 3-D network of pre-existing (prograde) biotite–sillimanite–mullite foliations. Post-garnet growth, extensional Mode I fractures formed due to local high melt pressure during veining stages of anatexis in combination with tectonic stresses. Microstructural analyses of garnet from the study hence imply that elongated shapes of peritectic garnets especially those crystallized in equilibrium with melts need not necessarily be due to ductile, crystal–plastic deformation and that under such conditions garnets may exhibit brittle behavior.

Near-random two weak CPOs of coarse-grained quartz in the matrix S<sub>2</sub> indicate that crystallization of melt outlasted high-temperature (>700 °C) D<sub>2</sub> deformation in these areas. Post-migmatization solid-state deformation was instead accommodated in the fine-grained quartz-rich domains interleaved with biotite, sillimanite, mullite in the S<sub>3</sub> layers. These layers represent restitic layers formed during partial melting. During post-migmatization deformation these phase-mixed, fine-grained layers act as rheological weak zones as they deform mainly by basal slip in biotite and rigid body rotation of both biotite and mullite and minor dislocation creep in quartz.

Our study suggests that the inferred rheological weakness of migmatites may outlast the actually melt-present time period, as biotite-\*rich layers developed during partial melting facilitates late-stage, solid-state deformation with low rheological strength.

**Acknowledgements** LS acknowledges Faculty Initiation Grant, IIT Roorkee for conducting field work and for the analytical costs. LS also acknowledges Dr. M. Satyanarayanan, NGRI, Hyderabad, India, for XRF analyses and Ms. Jyothirmayee Palaparthy for compiling the figures. SP acknowledges the Australian Research Council through her Future Fellowship (FT1101100070) for financial support. The authors thank one anonymous reviewer and Kåre Kullerud for their constructive reviews and Prof. Dullo for helpful editorship.

## Appendix

See Fig. 11.

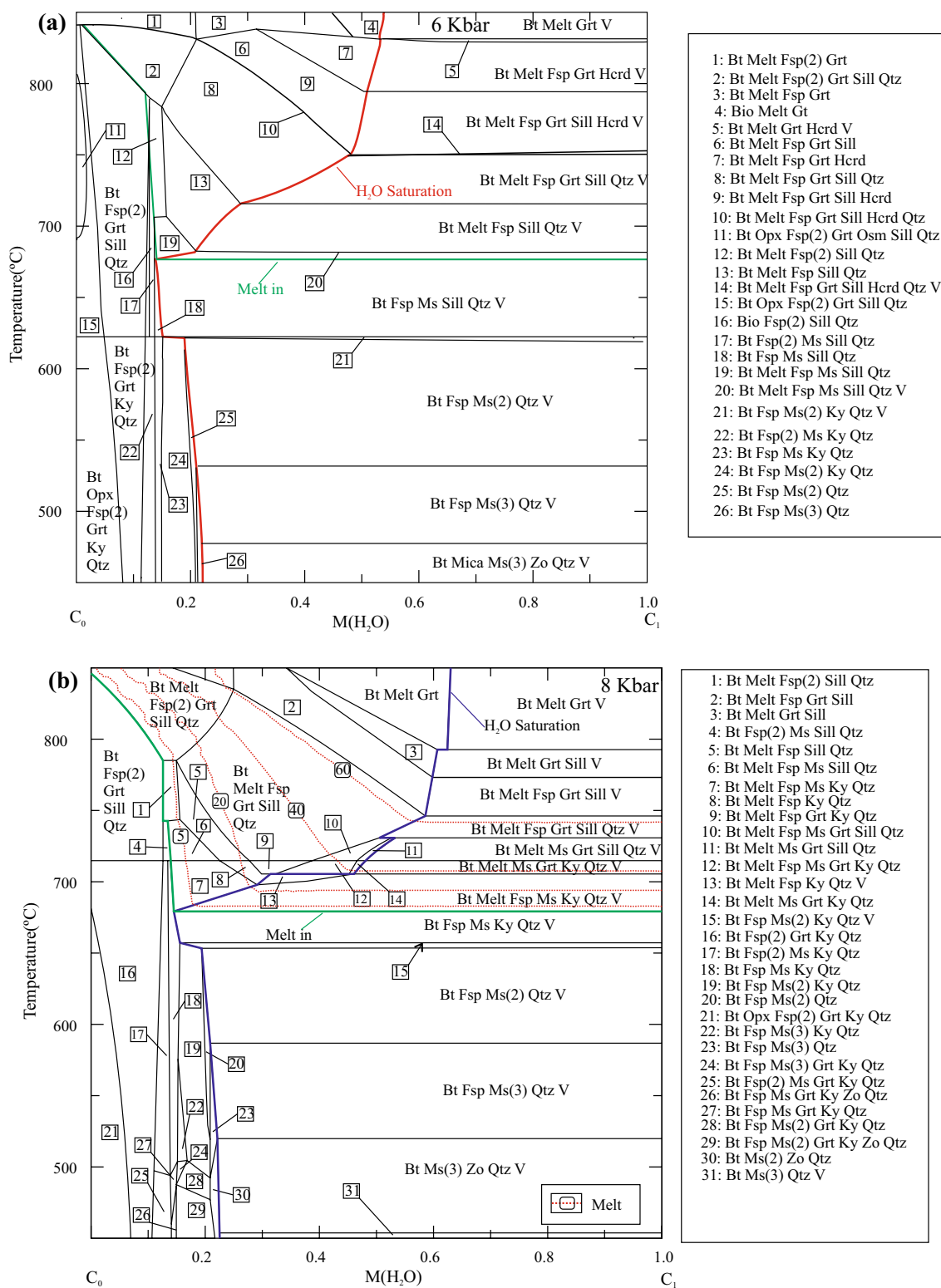


**Fig. 11 a, b** T–M<sub>H<sub>2</sub>O</sub> pseudosections at 6 and 8 kbar, respectively, showing stability fields of different minerals under water-deficient and water-fluxed conditions. High modal percentages of melt are observed in garnet–sillimanite–bioite–feldspar–quartz–melt-bearing

fields. Bulk compositions for C<sub>0</sub> and C<sub>1</sub> (in molar proportions) are, respectively, SiO<sub>2</sub>:Al<sub>2</sub>O<sub>3</sub>:FeO:MgO: CaO:Na<sub>2</sub>O:K<sub>2</sub>O:H<sub>2</sub>O=62.68:12.56:6.77:10.99:1.49:1.49: 3.77:0.26 and 41.18:8.25:4.45:7.22:0.98:0.98:2.47:34.46

## References

- Abe S, Urai JL (2012) Discrete element modelling of boudinage: Insights on rock rheology, matrix flow, and evolution of geometry. *J Geophys Res* 117:B01407
- Arzi AA (1978) Critical phenomena in the rheology of partially molten rocks. *Tectonophysics* 74:173–184
- Ashworth JR (1985) *Migmatites*. Blackie, Glasgow
- Auzanneau E, Schmidt MW, Vielzeuf D, Connolly JAD (2010) Titanium in phengite: a geobarometer for high temperature eclogites. *Contrib Mineral Petrol* 159:1–24
- Beaumont C, Nguyen MH, Jamieson RA, Ellis S (2006) Crustal flow modes in large hot orogens, in channel flow, ductile extrusion and exhumation in continental collision zones, vol 268. Law RD, Searle MP, Godin L (ed) Geological Society of London Special Publication, pp 91–145
- Behrmann J, Mainprice D (1987) Deformation mechanisms in a high-temperature quartz feldspar mylonite evidence for superplastic flow in the lower continental-crust. *Tectonophysics* 140:297–305
- Benisek A, Kroll H, Cemic L (2004) New developments in two-feldspar thermometry. *Am Mineral* 89:1496–1504
- Berger A, Kalt A (1999) Structures and melt fractions as indicators of rheology in cordierite-bearing migmatites of the Bayerische Wald (Variscan Belt, Germany). *J Petrol* 40:1699–1719
- Bestmann M, Prior DJ (2003) Intragranular dynamic recrystallization in naturally deformed calcite marble: diffusion accommodated grain boundary sliding as a result of subgrain rotation recrystallization. *J Struct Geol* 25:1597–1613
- Bhattacharya A, Mohanty L, Maji A, Sen SK, Raith M (1992) Non-ideal mixing in the phlogopite-annite boundary: constraints from experimental data on Mg–Fe partitioning and a reformulation of the biotite-garnet geothermometer. *Contrib Mineral Petr* 111:87–93
- Bhowmik SK, Bernhardt HJ, Dasgupta S (2010) Grenvillian age high-pressure upper amphibolite–granulite metamorphism in the Aravalli–Delhi Mobile Belt, North-western India: new evidence from monazite chemical age and its implication. *Precambrian Res* 178:168–184
- Brodie KH, Rutter EH (2000) Deformation mechanisms and rheology: why marble is weaker than quartzite. *J Geol Soc London* 157:1093–1096
- Brown M (2001) Orogeny, migmatites and leucogranites: a review. *Proc Indian Acad Sci (Earth Planet Sci)* 110:313–336
- Brown M (2002) Retrograde processes in migmatites and granulites revisited. *J Metamorph Geol* 20:25–40
- Buick IS, Allen C, Pandit M, Rubatto D, Hermann J (2006) The Proterozoic magmatic and metamorphic history of the Banded Gneiss Complex, central Rajasthan, India: LA-ICP-MS U–Pb zircon constraints. *Precambrian Res* 151:119–142
- Buick IS, Clark C, Rubatto D, Hermann J, Pandit MK, Hand M (2010) Constraints on the Proterozoic evolution of the Aravalli–Delhi Orogenic belt (NW India) from monazite geochronology and mineral trace element geochemistry. *Lithos* 120:511–528
- Blumenfeld P, Mainprice D, Bouchez JL (1986) C-slip in quartz from subsolidus deformed granite. *Tectonophysics* 127:97–115
- Cavalcante GCG, Egydio-Silva M, Vauchez A, Camps P, Oliveira E (2013) Strain distribution across a partially molten middle crust: Insights from the AMS mapping of the Carlos Chagas Anateixite, Araçuaí belt (East Brazil). *J Struct Geol* 55:79–100
- Coggon R, Holland TJB (2002) Mixing properties of phengitic micas and revised garnet-phengite thermobarometers. *J Metamorph Geol* 20:683–696
- Connolly JAD (2005) Computation of phase equilibria by linear programming: a tool for geodynamic modeling and its application to subduction zone decarbonation. *Earth Planet Sci Lett* 236:524–541
- Cyprych D, Piazzolo S, Wilson CJ, Luzin V, Prior DJ (2016) Rheology, microstructure and crystallographic preferred orientation of matrix containing a dispersed second phase: Insight from experimentally deformed ice. *Earth Planet Sci Lett* 449:272–281
- Dasgupta S, Sengupta P, Guha D, Fukuoka M (1991) A refined garnet–biotite Fe–Mg exchange geothermometer and its application in amphibolites and granulites. *Contrib Mineral Petrol* 109:130–137
- Deb M, Thorpe RI (2004) Geochronological constraints in the Precambrian geology of Rajasthan and their metallogenic implications. In: Deb M, Goodfellow WD (eds) *Sediment-hosted Lead–Zinc Sulphide Deposits; Attributes and Models of Some Major Deposits in India, Australia and Canada*. Narosa, New Delhi, pp 246–263
- Deb M, Thorpe RI, Cumming GL, Wagner PA (1989) Age, source and Strati-graphic implications of Pb isotope data for conformable, sediment-hosted, base-metal deposits in the Proterozoic Aravalli–Delhi Orogenic Belt, Northwestern India. *Precambrian Res* 43:1–22
- Engi M, Wersin P (1987) Derivation and application of a solution model for calcic garnet. *Schweizerische Mineralogische und Petrographische Mitteilungen* 67:53–73
- Ferry JM, Spear FS (1978) Experimental calibration of the partitioning of Fe and Mg between biotite and garnet. *Contrib Mineral Petrol* 66:113–117
- Guernina S, Sawyer EW (2003) Large-scale melt-depletion in granulite terranes: an example from the Archean Ashuanipi Subprovince of Quebec. *J Metamorph Geol* 21:181–201
- Gupta SN, Arora YK, Mathur RK, Iqbaluddin BP, Sahai TN, Sharma SB (1980) *Lithostratigraphic Map of the Aravalli Region*. Scale 1:100,000. Geological Survey of India, Calcutta
- Gupta P, Mathur YK, Iqbaluddin BP, Sahai TN, Sharma SB (1997) *Lithostratigraphic map of the Aravalli region, southern Rajasthan and northeastern Gujarat*. Geological Survey of India Publications, Jaipur
- Hasalová P, Schulmann K, Lexa O, Štípská P, Hrouda F, Ulrich S, Haloda J, Týcová P (2008) Origin of migmatites by deformation-enhanced melt infiltration of orthogneiss: a new model based on quantitative microstructural analysis. *J Metamorph Geol* 26:29–53
- Hasalová P, Weinberg RF, Macre C (2011) Microstructural evidence for magma confluence and reusage of magma pathways: implications for magma hybridization, Karakoram Shear Zone in NW India. *J Metamorph Geol* 29:875–900
- Hazarika P, Upadhyay D, Mishra B (2013) Contrasting geochronological evolution of the Rajpura–Dariba and Rampura–Agucha metamorphosed Zn–Pb deposit, Aravalli–Delhi Belt, India. *J Asian Earth Sci* 73:429–439
- Heron AM (1953) *Geology of central Rajasthan*. Mem Geol Surv India 79:339
- Holdaway MJ (2000) Application of new experimental and garnet Margules data to the garnet–biotite geothermometer. *Am Mineral* 85:881–892
- Holland TJB, Powell R (1998) An internally consistent thermodynamic data set for phases of petrological interest. *J Metamorph Geol* 16:309–343
- Holland T, Powell R (2001) Calculation of phase relations involving haplogranitic melts using an internally consistent thermodynamic dataset. *J Petrol* 42:673–683
- Ji SC, Martignole J (1994) Ductility of garnet as an indicator of extremely high-temperature deformation. *J Struct Geol* 16:985–996
- Ji SC, Saruwatari K, Mainprice D, Wirth R, Xu Z, Xia B (2003) Microstructures, petrofabrics and seismic properties of ultra high-pressure eclogites from Sulu region, China: implications for rheology

- of subducted continental crust and origin of mantle reflections. *Tectonophysics* 370:49–76
- Kelsey D, White R, Powell R (2005) Calculated phase equilibria in  $K_2O$ – $FeO$ – $MgO$ – $Al_2O_3$ – $SiO_2$ – $H_2O$  for silica-undersaturated sapphirine-bearing mineral assemblages. *J Metamorph Geol* 23:217–239
- Kilian R, Heilbronner R, Stünitz H (2011) Quartz grain size reduction in a granitoid rock and the transition from dislocation to diffusion creep. *J Struct Geol* 33:1265–1284
- Kleinschrodt R, Duyster JP (2002) HT-deformation of garnet: an EBSD study on granulites from Sri Lanka, India and the Ivrea Zone. *J Struct Geol* 24:1829–1844
- Kleinschrodt R, McGrew A (2000) Garnet plasticity in the lower continental crust: implications for deformation mechanisms based on microstructures and SEM-electron channeling pattern analysis. *J Struct Geol* 22:795–809
- Komoróczy A, Abe S, Urai JL (2013) Meshless numerical modeling of brittle–viscous deformation: first results on boudinage and hydrofracturing using a coupling of discrete element method (DEM) and smoothed particle hydrodynamics (SPH). *Comput Geosci* 17:373–390
- Kretz R (1983) Symbols for rock-forming minerals. *Am Mineral* 68:277–279
- Law RD (2014) Deformation thermometry based on quartz c-axis fabrics and recrystallization microstructures: a review. *J Struct Geol* 66:129–161
- Ludwig KR (2001) User manual for Isoplot/Ex ver. 2.49: A geochronological toolkit for Microsoft Excel. Berkeley Geochronol Centre Spec Publ 1a:1–56
- Mainprice D, Bascou J, Cordier P, Tommasi A (2004) Crystal preferred orientations of garnet: comparison between numerical simulations and electron back-scattered diffraction (EBSD) measurements in naturally deformed eclogites. *J Struct Geol* 26:2089–2102
- Menegon L, Nasipuri P, Stünitz H, Behrens H, Ravna E (2011) Dry and strong quartz during deformation of the lower crust in the presence of melt. *J Geophys Res* 116:B10410
- Nasipuri P, Bhattacharya A, Das S (2009) Metamorphic reactions in dry and aluminous granulites: a  $Perple\_X$  P–T pseudosection analysis of the influence of effective reaction volume. *Contrib Mineral Petrol* 157:301–311
- Ojha MK, Mishra B, Hazarika P, Jeyagopal AV, Yadav GS (2016) EPMA monazite geochronology of the basement and supracrustal rocks within the Pur-Banera basin, Rajasthan: evidence of Columbia breakup in Northwestern India. *J Asian Earth Sci* 117:284–303
- Passchier CW, Trouw RAJ (2005) *Microtectonics*. Springer, Berlin, p. 366
- Paterson MS (1987) Problems in the extrapolation of laboratory rheological data. *Tectonophysics* 133:33–43
- Petrík I, Konečný P (2009) Metasomatic replacement of inherited metamorphic monazite in a biotite–garnet granite from the Nízke Tatry Mountains, Western Carpathians, Slovakia: chemical dating and evidence for disequilibrium melting. *Am Mineral* 94:957–974
- Piazolo S, Jaconelli P (2013) Sillimanite deformation mechanisms within a Grt–Sil–Bt gneiss: effect of pre-deformation grain orientations and characteristics on mechanism, slip-system activation and rheology. *Geol Soc London Spec Publ* 394:189–213
- Piazolo S, Bestmann M, Spiess C, Prior DJ (2006) Temperature dependent grain boundary migration mechanisms: insights from insitu experiments. *Tectonophysics* 427:55–71
- Prior DJ, Boyle AP, Brenker F, Cheadle MC, Day A, Lopez G, Peruzzo L, Potts GJ, Reddy S, Spiess R, Timms NE, Trimby P, Wheeler J, Zetterstrom L (1999) The application of electron backscatter diffraction and orientation contrast imaging in the SEM to textural problems in rocks. *Am Mineral* 84:1741–1759
- Prior DJ, Wheeler J, Brenker FE, Harte B, Matthews M (2000) Crystal plasticity of natural garnet: new microstructural evidence. *Geology* 28:1003–1006
- Prior DJ, Wheeler J, Peruzzo L, Spiess R, Storey C (2002) Some garnet microstructures: an illustration of the potential of orientation maps and misorientation analysis in microstructural studies. *J Struct Geol* 24:999–1011
- Raja Rao CS (1976) Precambrian sequences of Rajasthan. *Misc Publ Geol Surv India* 23:497–516
- Rimsa A, Whitehouse MJ, Piazzolo S (2007) Brittle fracturing and fracture healing of zircon: integrated cathodoluminescence, U–Th–Pb and REE study. *Am Mineral* 92:1213–1224
- Roy AB (2000) Structural investigation of the Rampura–Agucha Mine and Neighbourhood. Hindustan Zinc Ltd. Project Report, p 30 (**unpublished**)
- Roy AB, Jakhar SR (2002) *Geology of Rajasthan (Northwest India) Precambrian to recent*. Scientific Publishers, Jodhpur
- Rutter E, Neumann DHK (1995) Experimental deformation of partially molten Westerly granite under fluid absent conditions, with implications for the extraction of granitic magmas. *J Geophys Res* 100:15697–15715
- Saha L, Bhowmik SK, Fukuoka M, Dasgupta S (2008) Contrasting episodes of regional granulite facies metamorphism in enclaves and host gneisses from the Aravalli–Delhi Mobile Belt, NW India. *J Petrol* 49:107–128
- Sawyer EW (2001) Melt segregation in the continental crust: distribution and movement of melt in anatectic rocks. *J Metamorph Geol* 19:291–309
- Sawyer EW (2008) *Atlas of migmatites*, vol 9. Mineralogical Associations of Canada Special Publication, p 387
- Schmid S (1982) Microfabric studies as indicators of deformation mechanisms and microfabric studies as indicators of deformation mechanisms and flow laws operative in mountain building. In: Hsu K (ed) *Mountain building processes*. Academic Press, London, pp 95–110
- Smith JR, Piazzolo S, Daczko NR, Evans L (2015) The effect of pre-tectonic reaction and annealing extent on behaviour during subsequent deformation: insights from paired shear zones in the lower crust of Fiordland, New Zealand. *J Metamorph Geol* 33:557–577
- Song WJ, Ree JH (2007) Effect of mica on the grain size of dynamically recrystallized quartz in a quartz–muscovite mylonite. *J Struct Geol* 29:1872–1881
- Spear FS (1993) *Metamorphic phase equilibria and pressure–temperature–time paths*. Mineralogical Society America Monograph, Book Crafters, Chelsea
- Storey CD, Prior DJ (2005) Plastic deformation and recrystallization of garnet: a mechanism to facilitate diffusion creep. *J Petrol* 46:2593–2613
- Stüwe K (1997) Effective bulk composition change due to cooling: a model predicting complexities in retrograde reaction textures. *Contrib Mineral Petrol* 129:43–52
- Stüwe K (2007) *Geodynamics of the lithosphere: quantitative description of geological problems*, 2nd edn. Springer, Berlin, p 493
- Svahnberg H, Piazzolo S (2010) The initiation of strain localisation in plagioclase-rich rocks: insights from detailed microstructural analyses. *J Struct Geol* 32:1404–1416
- Takeda Y–T, Obata M (2003) Some comments on the rheologically critical melt percentage. *J Struct Geol* 25:813–818
- Tomascak PB, Krogstad EJ, Walker RJ (1998) Sm–Nd isotope systematics and the derivation of granitic pegmatites in southwestern Maine. *Can Mineral* 36:327–337
- Tretiakova IG, Belousova EA, Malkovets VG, Griffin WL, Piazzolo S, Pearson NJ, O’Reilly SW, Nishido H (2016) Recurrent magmatic activity on a lithosphere-scale structure: crystallization and deformation in kimberlitic zircons. *Gondwana Res* 42:126–132



- Venables JA, Harland CJ (1973) Electron back-scattering patterns—a new technique for obtaining crystallographic information in the SEM. *Philos Mag* 27:1193–1200
- Vignerresse JL, Barbey P, Cuney M (1996) Rheological transitions during partial melting and crystallization with application to felsic magma segregation and transfer. *J Petrol* 37:1579–1600
- Webb G, Powell R, McLaren S (2015) Phase equilibria constraints on the melt fertility of crustal rocks: the effect of subsolidus water loss. *J Metamorph Geol* 33:147–165
- White RW, Powell R (2002) Melt loss and the preservation of granulite facies mineral assemblages. *J Metamorph Geol* 20:621,632
- White RW, Powell R (2010) Retrograde melt-residue interaction and the formation of near-anhydrous leucosomes in migmatites. *J Metamorph Geol* 28:579–597
- White RW, Powell R, Holland TJB (2001) Calculation of partial melting equilibria in the system  $\text{Na}_2\text{O}-\text{CaO}-\text{K}_2\text{O}-\text{FeO}-\text{MgO}-\text{Al}_2\text{O}_3-\text{SiO}_2-\text{H}_2\text{O}$  (NCKFMASH). *J Metamorph Geol* 19:139–153
- White RW, Powell R, Holland TJB (2007) Progress relating to calculations of partial melting equilibria for metapelites. *J Metamorph Geol* 25:511–527
- Whitney D, Teyssier C, Vanderhaeghe O (2004) Gneiss domes and crustal flow. *Geol Soc Am Spec Papers* 380:15–330